Peridynamic modeling of elastic bimaterial interface fracture

Heng Zhang[a], Xiong Zhang[a,*], Yan Liu[a], Pizhong Qiao[b]

[a] *School of Aerospace Engineering, Tsinghua University, Beijing 100084, China*
[b] *State Key Laboratory of Ocean Engineering, School of Naval Architecture, Ocean and Civil Engineering, Shanghai Jiao Tong University, Shanghai, 200240, China*

Abstract

A general peridynamics-based framework for elastic bimaterial interface fracture analysis is established. In this frame, the formation of peridynamic interface bond force is presented for nonlocal interface modeling, and the energy release rate and mode mixity of interface cracks are computed with peridynamic model. A modified critical energy density (MCED) criterion considering both interfacial and materials fracture toughness is proposed for peridynamic bond failure analysis, and the bond failure competition strategy is considered for crack path selection of an interface crack along or kinking out of the interface. Then, four tests of a bimaterial plate under uniform tensile stress, asymmetric bimaterial cantilever beams (ABCB), bimaterial single edge notched (BSEN) and four-point shearing (FPS) tests are investigated for the model verification and application. The deformation and fracture behaviors of these specimens are predicted with the proposed peridynamic models, and compared to those from FEM, theoretical and experimental solutions. The results show that the proposed peridynamics-based method can successfully capture the characteristics of bimaterial interface fracture, including the delamination fracture, kinking nucleation and crack path selection of interface cracks.

1. Introduction

Bimaterial interfaces are commonly contained in layered systems, such as laminated composite, adhesive joints and metal–ceramics. Due to the material discontinuity across these interfaces, the interface fracture is one of the most common failure modes of layered systems. Thus, the better understanding and prediction of bimaterial interface fracture are crucial for the service life and structure design of layered materials and structures.

An interface crack contained between two dissimilar elastic materials has been widely studied (see Fig. 1). In fracture mechanic theory, the asymptotic stress and displacement fields around the interface crack were analyzed [1,2], and the fracture criteria were presented with the stress intensity factor solutions [3,4]. The interface crack path selection between different directions was also studied, and crack kinking out of an interface was investigated [5]. Generally, analytical solutions show that the material discontinuity in bimaterial interface can lead to the crack tip stress oscillation singularity, and the interface crack faces may be embedded into each other. These

---

* Corresponding author.
E-mail addresses: hengzh@tsinghua.edu.cn (H. Zhang), xzhang@tsinghua.edu.cn (X. Zhang).
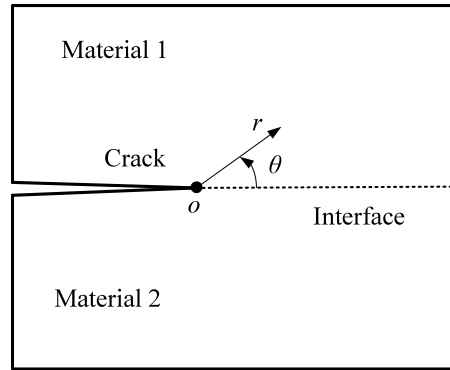
Fig. 1. An interface crack contained between two dissimilar materials.

factors display the difficulty of interface fracture problems and also restrict the application of the analytical methods. Meanwhile, the numerical model, the Finite Element Method (FEM) shows great achievement on stress field prediction in bimaterial systems [6]. Using the virtual crack closure technique (VCCT) [7] and the cohesive zone model (CZM) [8,9], FEM models have also been performed for the energy release rate computation and interface delamination modeling. However, their results are highly sensitive to mesh. Especially for crack kinking problems, since the kinking angle is unknown, remeshing is required and the complex fracture criteria are needed [10].

Nonlocal theory of peridynamics, as a reformulation of continuous mechanics, was first proposed in 2000 [11], in which the integral–differential motion equations are utilized instead of partial-differential equations. Thus, in peridynamic theory, the inadequacies of classical local theory for the discontinuous problems are removed, and the crack prediction problems, such as interface delamination and crack kinking, can be naturally solved without preset crack path and extra fracture criteria. The bond-based peridynamic (BB-PD) model was firstly proposed as the original version, in which the points are connected with bonds through spring-like interactions and the force response in a bond is dependent only on its own deformation. However, this assumption has restrictions on material parameter values, i.e., the Poisson's ratio limits to be 1/3 for the two-dimensional (2D) plane stress and 1/4 for the plane strain and three-dimension (3D) cases [12]. To handle these Poisson's ratio limitations, some extended BB-PD models have been proposed by incorporating with bond rotation effect [13,14], which also increases the complexity of the BB-PD model. The state-based peridynamics (SB-PD) [15] was proposed as a more general frame, in which the bond force density between points depends on the deformation of their whole family. Additionally, the SB-PD can be further classified into two types: ordinary state-based peridynamics (OSB-PD) [15,16] and non-ordinary state-based peridynamics (NOSB-PD) [17]. In the ordinary state-based (OSB-PD) model, the deformation can be explicitly employed as the volumetric and distortional parts for material response, and material behaviors in conventional solid mechanics can be reproduced, for not only linear elastic material [15], but also plastic [18,19], viscoelastic [20], and viscoplastic materials [21].

Meanwhile, bond failure criteria, as the foundation of peridynamics-based method for fracture analysis, have been successively proposed, in which the critical stretch-based [12,22] and critical energy density-based bond failure criteria [23] are the two most common models. For the mode II and mixed-mode fracture analysis, the critical skew [24] and mixed-mode bond failure models [25] were proposed. The failure models considering both stress and energy conditions were also presented [26–28]. Meanwhile, the fracture mechanic theories have been reformulated in peridynamics for energy release rate computation and fracture analysis, such as the J-integral [29,30], crack extension technique [31], virtual crack closure technique [32], and cohesive zone model [33–35].

Due to these advantages on discontinuity modeling, the peridynamic theory has been successfully used for failure predictions of various materials, such as concretes [36–39], composite materials [40–42] and rocks [43,44]. And it also has been applied for the bimaterial interface analysis. Alali et al. [45] and Seleson et al. [46] investigated the material interface in peridynamic theory and performed the convergence study of their peridynamic interface models. Wang et al. [47] and Zhang et al. [48] analyzed the deformation and failure of bimaterial structure, in which original bond failure models of the homogeneous materials were adopted. However, in above studies, some deficiencies remain for peridynamics-based bimaterial elastic and fracture analysis. First, for bimaterial elastic
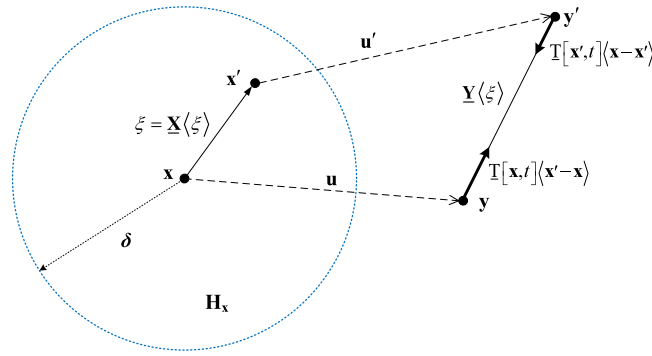
Fig. 2. Ordinary state-based peridynamic model.

behaviors modeling, the explicit form of peridynamic interface bond force for nonlocal interface is not given. While for bimaterial fracture analysis, there is no a typical bond failure model considering both interfacial and materials fracture toughness, and the mode mixity of interface cracks have also not been considered.

In this paper, a general peridynamics-based framework for bimaterial interface fracture analysis is established. First, forms of the peridynamic force state and interface bond force are presented for bimaterial elastic behaviors modeling. The peridynamics-based methods for interface crack energy release rate and mode mixity computations are given, and a modified critical energy density (MCED) criterion considering both interfacial and materials fracture toughness is proposed for bonds failure analysis. Then, four cases, i.e., a bimaterial plate under uniform tensile stress load, asymmetric bimaterial cantilever beams (ABCB), bimaterial single edge notched (BSEN) and four-point shearing (FPS) tests, are analyzed for the model verification and application, in which the delamination fracture and kinking nucleation of interface cracks are all investigated. The deformation and fracture behaviors of these tests are predicted with the proposed peridynamic model, and compared to those from FEM and theoretical solutions and experimental data.

2. Nonlocal interface model in peridynamics

In nonlocal peridynamic theory, the continuous system is divided into finite material points, and these points interact with each other by the peridynamic 'bonds'. The motion equation of a material point $\mathbf{x}$ can be expressed as [15]:

$$\rho\left(\mathbf{x}\right)\ddot{\mathbf{u}}\left(\mathbf{x}, t\right) = \int_{H_{\mathbf{x}}}\left\{\underline{\mathbf{T}}\left[\mathbf{x}, t\right]\langle\mathbf{x}' - \mathbf{x}\rangle - \underline{\mathbf{T}}\left[\mathbf{x}', t\right]\langle\mathbf{x} - \mathbf{x}'\rangle\right\}dV_{\mathbf{x}'} + \mathbf{b}\left(\mathbf{x}, t\right) \tag{1}$$

where ρ is the density of point $\mathbf{x}$, $\mathbf{u}$ is its displacement at time t, $H_{\mathbf{x}}$ is the neighborhood of point $\mathbf{x}$ with the cut-off radius of nonlocal horizon δ, $\mathbf{x}'$ is the neighbor point in $H_{\mathbf{x}}$, and $\mathbf{b}\left(\mathbf{x}, t\right)$ is the body force density. $\boldsymbol{\xi} = \mathbf{x}' - \mathbf{x}$ is the bond vector as shown in Fig. 2, $\underline{\mathbf{X}}\langle\boldsymbol{\xi}\rangle$ and $\underline{\mathbf{Y}}\langle\boldsymbol{\xi}\rangle$ are the reference and deformed vectors of bond $\boldsymbol{\xi}$, and $\underline{\mathbf{T}}\left[\mathbf{x}, t\right]$ and $\underline{\mathbf{T}}\left[\mathbf{x}', t\right]$ are the force vector states of points $\mathbf{x}$ and $\mathbf{x}'$, respectively. In the ordinary state-based peridynamic theory, the bond force vector can be expressed with the force scalar state $\underline{t}$ as [15]:

$$\underline{\mathbf{T}}\left[\mathbf{x}, t\right]\langle\boldsymbol{\xi}\rangle = \underline{t}\langle\boldsymbol{\xi}\rangle\frac{\underline{\mathbf{Y}}\langle\boldsymbol{\xi}\rangle}{\left|\underline{\mathbf{Y}}\langle\boldsymbol{\xi}\rangle\right|} \tag{2}$$

2.1. Peridynamic scalar force states in bimaterial system

In a bimaterial structure, as shown in Fig. 3, two different materials are connected with an interface, and the interface is assumed as zero thickness. For this bimaterial system modeling, the material points in peridynamics are naturally classified into two types that belong to material 1 or material 2. For example, point $\mathbf{x1}$ belongs to material 1, points $\mathbf{x2}$ and $\mathbf{x3}$ belong to material 2 (see Fig. 3). And $H_{\mathbf{x}_i}$ is the neighborhood horizon of point $\mathbf{x}_i$ with the same cut-off radius δ.
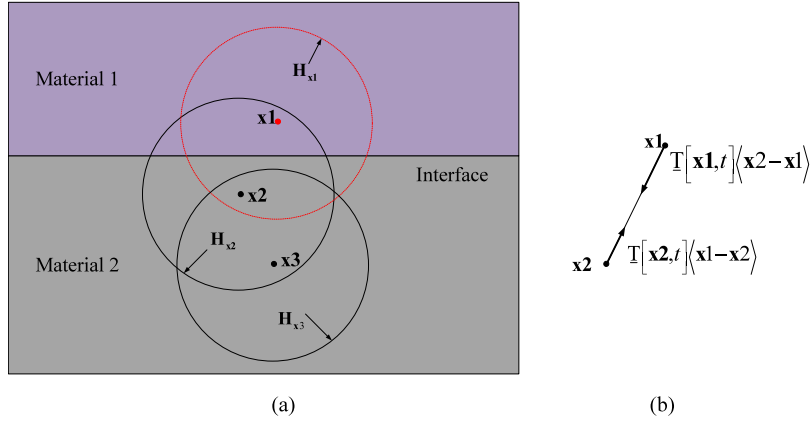
(a)   (b)

Fig. 3. Peridynamic bimaterial system: (a) different types of material points and their horizons, (b) the bond force of the interface bond between points **x1** to **x2**.

In the ordinary state-based model, the scalar force state $\underline{t}$ of the points belong to the linear elastic isotropic material i takes the form of [16]:

$$\underline{t} = \begin{cases} 3\left(k_i' - \dfrac{5\mu_i}{3}\right)\theta\dfrac{\underline{\omega x}}{q} + \dfrac{15\mu_i}{q}\underline{\omega e}; & 3D \\ 2\left(k_i' - 2\mu_i\right)\theta\dfrac{\underline{\omega x}}{q} + \dfrac{8\mu_i}{q}\underline{\omega e}; & 2D \\ \dfrac{E_i}{q}\underline{\omega e}; & 1D \end{cases} \tag{3}$$

where $\underline{\omega}$ is the influence function, $\underline{x}$ is equal to bond length $|\boldsymbol{\xi}|$, q is the weighted volume that is defined as $\underline{\omega x} \bullet \underline{x}$, $\underline{e}$ is the extension state, and θ is the volume dilatation that can be obtained with:

$$\begin{cases} \theta = 3\dfrac{\underline{\omega x} \bullet \underline{e}}{q}; & 3D \\ \theta = 2\dfrac{\underline{\omega x} \bullet \underline{e}}{q}; & 2D \\ \theta = \dfrac{\underline{\omega x} \bullet \underline{e}}{q}; & 1D \end{cases} \tag{4}$$

where the symbol ($\bullet$) is the dot product operation [15], μ_i is the shear modulus of material i, and k_i' is the bulk modulus that can be expressed as:

$$k_i' = \begin{cases} \dfrac{E_i}{3(1 - 2v_i)} & 3D \\ \dfrac{E_i}{2(1 - v_i)} & \text{Plane stress} \\ \dfrac{E_i}{2(1 + v_i)(1 - 2v_i)} & \text{Plane strain} \end{cases} \tag{5}$$

where E_i and v_i are the Young's modulus and Poisson's ratio of material i, respectively.

In this peridynamic bimaterial model, since horizons of the points near material interface cover both material 1 and material 2 zones (see Fig. 3(a)), the points in different materials can interact each other with their connected bonds, called as 'peridynamic interface bonds' (see Fig. 3(b)). Thus, even though the material interface is not explicitly revealed, the interior force can be transmitted through nonlocal interface by these peridynamic interface bonds. In other words, though the force state of point **x1** is computed with parameters of material 1, the deformation states of point **x1** (i.e. volume dilatation θ and extension state $\underline{e}$) are captured via all deformation of its horizon $H_{\mathbf{x1}}$, part of which is located in material 2 zone (see Fig. 3(a)).

2.2. The bond force of the peridynamic interface bond

As shown in Fig. 3(b), the bond force of point **x1** effected by **x2** through their connected interface bond is:

$$\mathbf{f}[\mathbf{x}1, t]\langle\mathbf{x}2 - \mathbf{x}1\rangle = \underline{\mathbf{T}}[\mathbf{x}1, t]\langle\mathbf{x}2 - \mathbf{x}1\rangle - \underline{\mathbf{T}}[\mathbf{x}2, t]\langle\mathbf{x}1 - \mathbf{x}2\rangle \tag{6}$$

Considering Eq. (2), Eq. (6) can be further expressed as:

$$\mathbf{f}[\mathbf{x}1, t]\langle\mathbf{x}2 - \mathbf{x}1\rangle = \left(\underline{t}[\mathbf{x}1]\langle\mathbf{x}2 - \mathbf{x}1\rangle + \underline{t}[\mathbf{x}2]\langle\mathbf{x}1 - \mathbf{x}2\rangle\right)\frac{\underline{\mathbf{Y}}\langle\mathbf{x}2 - \mathbf{x}1\rangle}{\left|\underline{\mathbf{Y}}\langle\mathbf{x}2 - \mathbf{x}1\rangle\right|} \tag{7}$$

where $\underline{t}[\mathbf{x}1]$ and $\underline{t}[\mathbf{x}2]$ are the force scalar states of points **x1** and **x2**, which belong to material 1 and 2, respectively (see Fig. 3(a)), and they can be computed by Eq. (3).

Similarly, the bond force of point **x2** effected by **x1** is:

$$\mathbf{f}[\mathbf{x}2, t]\langle\mathbf{x}1 - \mathbf{x}2\rangle = \left(\underline{t}[\mathbf{x}1]\langle\mathbf{x}2 - \mathbf{x}1\rangle + \underline{t}[\mathbf{x}2]\langle\mathbf{x}1 - \mathbf{x}2\rangle\right)\frac{\underline{\mathbf{Y}}\langle\mathbf{x}1 - \mathbf{x}2\rangle}{\left|\underline{\mathbf{Y}}\langle\mathbf{x}1 - \mathbf{x}2\rangle\right|} = -\mathbf{f}[\mathbf{x}1, t]\langle\mathbf{x}2 - \mathbf{x}1\rangle \tag{8}$$

Thus, the linear admissibility condition for interacted force of the peridynamic interface bond is satisfied, and it can further ensure the balance of linear momentum condition of bimaterial system. In addition, considering the property of ordinary state-based model in Eq. (2), the balance of angular momentum can also be satisfied [15].

Typically, considering the Poisson's ratio restrictions in bond-based peridynamic model, and using the typical influence function of $\underline{\omega} = \delta/|\boldsymbol{\xi}|$, the scalar force state $\underline{t}$ of points in material i can be reduced into [22]:

$$\underline{t} = \frac{1}{2}c_i\underline{s} \tag{9}$$

where $\underline{s}$ is the bond stretch scalar state defined as $\underline{s} = \underline{e}/|\boldsymbol{\xi}|$, and c_i is the peridynamic constant of material i in bond-based peridynamic model [22], which can be expressed as:

$$c_i = \begin{cases} \dfrac{18k_i'}{\pi\delta^4}; & \text{3D} \\[2mm] \dfrac{12k_i'}{\pi\delta^3 B}; & \text{2D} \\[2mm] \dfrac{2E_i}{\delta^2 A}; & \text{1D} \end{cases} \tag{10}$$

where k_i' is the bulk modulus given in Eq. (5), B and A are the thickness and cross section for the 2D and 1D cases, respectively. Then, the interacted force of the peridynamic interface bond can be rewritten as:

$$\mathbf{f}[\mathbf{x}1, t]\langle\mathbf{x}2 - \mathbf{x}1\rangle = \frac{1}{2}(c_1 + c_2)\underline{s}\langle\mathbf{x}2 - \mathbf{x}1\rangle\frac{\underline{\mathbf{Y}}\langle\mathbf{x}2 - \mathbf{x}1\rangle}{\left|\underline{\mathbf{Y}}\langle\mathbf{x}2 - \mathbf{x}1\rangle\right|} \tag{11}$$

which is equal to the bond-based peridynamic interface model in [46].

2.3. The nonlocal property of peridynamic interface model

Here, one-dimensional (1D) peridynamic bimaterial bar is considered to investigate the nonlocal property of proposed peridynamic interface model (see Fig. 4).

As shown in Fig. 4, the bar with uniform cross section A is connected by zero thickness interface, and the linear elastic isotropic material 1 and material 2 are considered in left and right sides of the interface. For a material point **p** in this peridynamic bimaterial bar, the stress $\boldsymbol{\sigma}(\mathbf{p})$ is defined as the total force that all its right points **x** exert on all its left points **x'** [49]:

$$\boldsymbol{\sigma}(\mathbf{p}) = \frac{1}{A}\int_0^\delta\int_0^{\delta - s}\mathbf{f}[\mathbf{x}, t]\langle\mathbf{x'} - \mathbf{x}\rangle A\,dr\,A\,ds = \int_0^\delta\int_0^{\delta - s}\mathbf{f}[\mathbf{x}, t]\langle\mathbf{x'} - \mathbf{x}\rangle A\,dr\,ds \tag{12}$$

where $\mathbf{f}[\mathbf{x}, t]$ is bond force that can be computed from Eq. (11).

When a uniform deformation of $u(x) = \varepsilon_0 x$ is applied in this bar, the scalar value of Eq. (12) can be computed and simplified as:
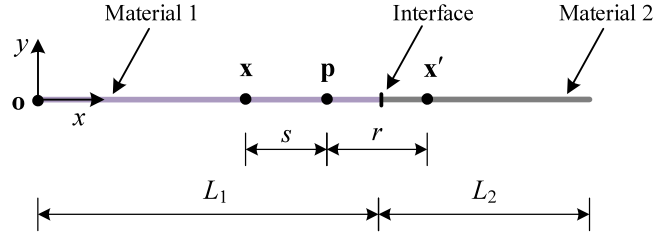
$$\sigma(\mathbf{p}) = E'\varepsilon_0 \tag{13}$$

Fig. 4. The point **p** in the one-dimensional peridynamic bimaterial bar.
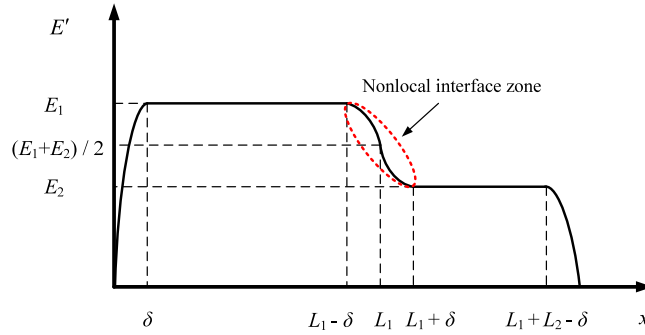

Fig. 5. The equivalent nonlocal elastic modulus in one-dimensional (1D) peridynamic bimaterial model.

where the equivalent nonlocal elastic modulus $E' = \sigma(\mathbf{p})/\varepsilon_0$ is defined to embody the property of peridynamic bimaterial model. Apply the integration in Eq. (12), the formation of E' can then be obtained as:

$$
E' = \begin{cases}
E_1\left(2\dfrac{x}{\delta} - \dfrac{x^2}{\delta^2}\right) & 0 \le x < \delta \\[2mm]
E_1 & \delta \le x < L_1 - \delta \\[2mm]
\dfrac{1}{2}(E_1 + E_2) + \dfrac{1}{2}(E_1 - E_2)\left(2\dfrac{(L_1 - x)}{\delta} - \dfrac{(L_1 - x)^2}{\delta^2}\right) & L_1 - \delta \le x < L_1 \\[2mm]
\dfrac{1}{2}(E_1 + E_2) + \dfrac{1}{2}(E_1 - E_2)\left(2\dfrac{(L_1 - x)}{\delta} + \dfrac{(L_1 - x)^2}{\delta^2}\right) & L_1 \le x < L_1 + \delta \\[2mm]
E_2 & L_1 + \delta \le x < L_1 + L_2 - \delta \\[2mm]
E_2\left(2\dfrac{(L_1 + L_2 - x)}{\delta} - \dfrac{(L_1 + L_2 - x)^2}{\delta^2}\right) & L_1 + L_2 - \delta \le x \le L_1 + L_2
\end{cases}
\tag{14}
$$

Meanwhile, the distribution of E' related to the location x is presented in Fig. 5. As shown, unlike the parameter value jump on material interface and boundary in continuum mechanics, the function of E' has the one-order continuity in whole peridynamic bimaterial bar of $0 \le x \le L_1 + L_2$. Typically, the nonlocal interface zone exists between $L_1 - \delta \le x < L_1 + \delta$, in which E' quadratically changes from $L_1 - \delta$ to L_1 and then L_1 to $L_1 + \delta$ in different functions. E' decreases to 0 as x approaches two boundaries, which shows the surface effect of peridynamic theory [50]. Additionally, when the value of horizon δ converges to 0, the nonlocal zone of E' gradually decreases, and the peridynamic bimaterial model would converge to classical mechanic theory.

Thus, the nonlocal property of peridynamic theory can cause the smearing effect of the material parameter in the bimaterial interface, which would reduce the deformation discontinuity near the interface.
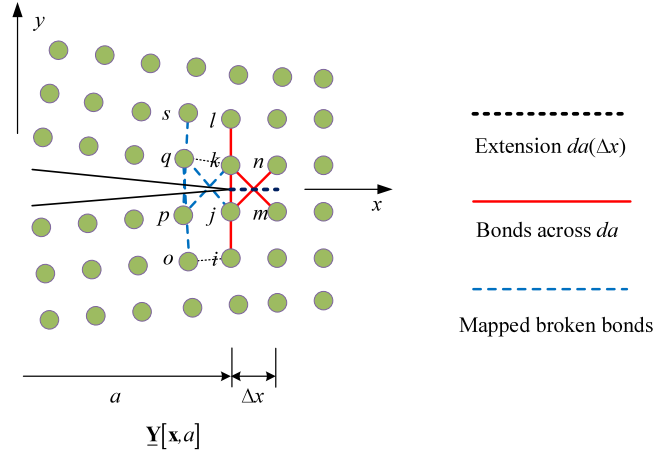
Fig. 6. Virtual crack closure technique in discrete peridynamic model with typical value of $m = 2$. The bond across the crack extension da maps to its corresponding bond behind.

3. Energy release rate and mode mixity of the interface crack in peridynamics

The energy release rate (ERR) and mode mixity are essential and significant parameters to characterize an interface crack, and the peridynamics-based methods are presented for their values computation.

3.1. ERR computation in peridynamics

Recently, the virtual crack closure technique was reformulated by Zhang and Qiao [32] in peridynamic theory, as the PD_VCCT, for the ERR calculation in the framework of peridynamics.

As shown in Fig. 6, in the PD_VCCT method, the numerical total energy release rate can be expressed as:

$$\overline{G}(a) = \frac{1}{\Delta x} \sum_{\xi_{ik} \in S_\xi, \xi_{ik} \to \xi_{oq}} \left(\frac{1}{2} \left\{ \underline{t} \langle \mathbf{x}_k - \mathbf{x}_i \rangle + \underline{t}' \langle \mathbf{x}_i - \mathbf{x}_k \rangle \right\} \bullet \underline{e} \langle \mathbf{x}_q - \mathbf{x}_o \rangle \right) V_i V_k \tag{15}$$

where the discrete peridynamic numerical model with typical value of $m = 2$ is considered, Δx is the crack extension length, S_ξ is the set of all bonds across the crack extension da, ξ_{oq} is the corresponding bond mapped of bond ξ_{ik}, $\underline{t}$ and $\underline{t}'$ are the force scalar states of points $\mathbf{x}$ and $\mathbf{x}'$, respectively, $\underline{e}$ is the extension scalar state, and V_i and V_k are volumes of nodes $\mathbf{x}_i$ and $\mathbf{x}_k$, respectively.

In the mixed mode fracture, for the homogeneous isotropic materials, the ERR in Eq. (15) can be expressed as the summation of the mode I and mode II $\overline{G}(a) = \overline{G}_I(a) + \overline{G}_{II}(a)$. Thus, the displacement near the crack tip can be analytically separated into two components $\mathbf{u}^I$ and $\mathbf{u}^{II}$, for mode I and mode II, respectively [51]. For example, the displacement $\mathbf{u}_i$ of point x_i can be divided into the symmetric and antisymmetric parts with the displacement of its mirror symmetric point x_l (see Fig. 7):

$$\mathbf{u}_i = \mathbf{u}_i^I + \mathbf{u}_i^{II} = \frac{1}{2} \begin{Bmatrix} u_{ix} + u_{lx} \\ u_{iy} - u_{ly} \end{Bmatrix} + \frac{1}{2} \begin{Bmatrix} u_{ix} - u_{lx} \\ u_{iy} + u_{ly} \end{Bmatrix} \tag{16}$$

Using the separated deformations $\mathbf{u}^I$ and $\mathbf{u}^{II}$ for mode I and mode II, the corresponding extension scalar states $\underline{e}^I[\mathbf{x}, a]$ and $\underline{e}^{II}[\mathbf{x}, a]$, and the force vector states $\underline{\mathbf{T}}^I[\mathbf{x}, a]$ and $\underline{\mathbf{T}}^{II}[\mathbf{x}, a]$ can be respectively obtained. Then, the numerical mode I and mode II ERRs for mixed mode crack can be obtained as:

$$\overline{G}_{Mode}(a) = \frac{1}{\Delta x} \sum_{\xi_{ik} \in S_\xi, \xi_{ik} \to \xi_{oq}} \left(\frac{1}{2} \left\{ \underline{t}^{Mode} \langle \mathbf{x}_k - \mathbf{x}_i \rangle + \left(\underline{t}' \right)^{Mode} \langle \mathbf{x}_i - \mathbf{x}_k \rangle \right\} \cdot \underline{e}^{Mode} \langle \mathbf{x}_q - \mathbf{x}_o \rangle \right) V_i V_k \tag{17}$$

where $Mode = I$ or II.

Similarly to the finite element method (FEM) based-VCCT, the G_I and G_{II} from Eq. (17) do not have unique values for bimaterial interface cracks because of the material mismatch. The values of G_I and G_{II} depend on the
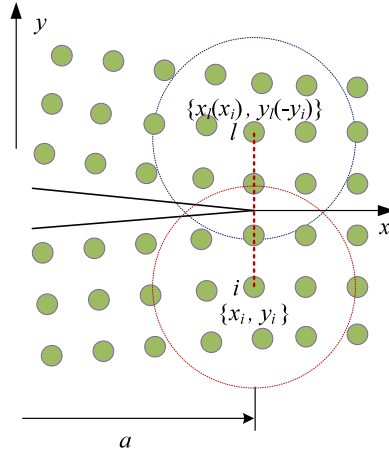
Fig. 7. Mirror points i and l with respect to x axis (crack surface) in discrete peridynamic model.

crack extension size Δx as well as the nonlocal horizon δ, and do not converge as Δx converges to infinitesimal value. Anyway, the value of total energy release rate is still unique.

3.2. ERR-based mode mixity in peridynamics

A crack constrained in the interface is mostly in mixed mode condition, and the mode mixity of interface cracks has a great effect on the interfacial fracture toughness and crack growth characteristics [7]. Here, the peridynamics-based method is proposed for the mode mixity computation of interface cracks.

Based on the energy release rate (ERR), the mode mixity, ψ_G, can be defined as:

$$\tan^2 \psi_G = \frac{G_{II}}{G_I} \tag{18}$$

where G_I and G_{II} are the mode I and II ERRs obtained from Eq. (17). For a crack in the homogeneous materials, the solution of ERR-based mode mixity is unique. However, for a bimaterial interface crack, since the values of ERRs are mesh-dependent, the mode mixity, ψ_G, also depends on the mesh grid size Δx.

The mesh-independent ERR-based mode mixity, ψ, was defined and computed as a correction of ψ_G by introducing a normalizing length parameter l in [7], in which oscillating ERRs from the FEM_VCCT were utilized. The same method can be performed in peridynamics to obtain the mesh-independent mode mixity ψ with the reference length l and the mesh grid size Δx. Furthermore, this computed mode mixity obeys the bimaterial phase change law as [7]:

$$\psi_0 = \psi + \varepsilon \ln \frac{l_0}{l} \tag{19}$$

where ε is the bimaterial constant defined in [7], l_0 and l are two reference lengths for the mode mixities ψ_0 and ψ, respectively.

4. Bimaterial interface fracture in peridynamics

In this section, for bimaterial interface fracture analysis, the peridynamic interface and interior bonds are identified, a modified critical bond energy density (MCED)-based criterion is proposed for these bonds failure analysis, and crack path competition of an interface crack along or kinking out of the interface is discussed.

4.1. Peridynamic bonds in bimaterial system

As a crack constrained in the bimaterial interface, the interfacial crack tip is mostly under the mixed mode condition if the crack keeps growing along the interface; while the advancing crack tip tends to be in mode I when the crack kinks out the interface and grows inside the materials [3].
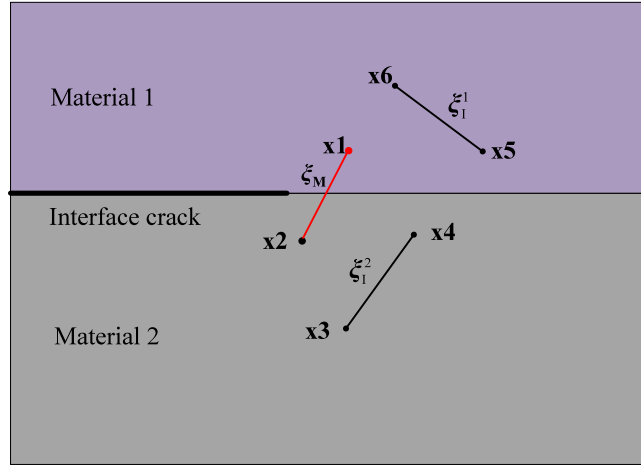
Fig. 8. Two kinds of peridynamic bonds in the bimaterial model: $\xi_{\mathbf{M}}$ for the interface interaction (red line), $\boldsymbol{\xi}_{\mathbf{I}}^{1}$ and $\boldsymbol{\xi}_{\mathbf{I}}^{2}$ for the interior interactions inside the material 1 and 2 (black line).

Thus, for bimaterial fracture modeling, the bonds in peridynamic bimaterial model are divided into two kinds (see Fig. 8): all bonds across the bimaterial interface are identified as the peridynamic interface bonds $\xi_{\mathbf{M}}$; while the other bonds inside material 1 and 2 are identified as the interior bonds $\boldsymbol{\xi}_{\mathbf{I}}^{1}$ and $\boldsymbol{\xi}_{\mathbf{I}}^{2}$. Since the mode condition and fracture property of cracks in the bimaterial interface and relative isotropic materials are different, a modified bond failure criterion is defined for these bonds failure prediction.

4.2. Modified critical energy density (MCED)-based bond failure criterion

The bond energy density was first defined in the energy-based bond failure criterion [23]. In the ordinary state-based peridynamics, considering the dual force density property and the linear elastic property, the bond energy density can be simplified into [16]:

$$\underline{w}\langle\boldsymbol{\xi}\rangle = \frac{1}{2}\left(\underline{t}\langle\boldsymbol{\xi}\rangle + \underline{t}'\langle\boldsymbol{\xi}\rangle\right)\cdot\underline{e}\langle\boldsymbol{\xi}\rangle \tag{20}$$

where $\underline{e}\langle\boldsymbol{\xi}\rangle$ is the extension scalar of bond $\boldsymbol{\xi}$, $\underline{t}\langle\boldsymbol{\xi}\rangle$ and $\underline{t}'\langle\boldsymbol{\xi}\rangle$ are the force scalar of points $\mathbf{x}$ and $\mathbf{x}'$, respectively (see Fig. 2).

Here, the modified critical energy density (MCED) $\underline{w}_c\langle\boldsymbol{\xi}\rangle$ is defined for failure prediction of the interface bond $\xi_{\mathbf{M}}$ and interior bond $\boldsymbol{\xi}_{\mathbf{I}}^{i}$ ($i = 1, 2$). Considering the fracture energy equivalence in [24], the total bond released energy at unit area of interface crack or interior crack is equal to the interfacial fracture toughness or materials critical energy release rate, respectively. Thus, the MCED of the interface bond $\xi_{\mathbf{M}}$ and interior bond $\boldsymbol{\xi}_{\mathbf{I}}^{i}$ can be obtained as:

$$\underline{w}_c\langle\boldsymbol{\xi}_{\mathbf{M}}\rangle = \begin{cases} \dfrac{4\Gamma(\psi_0)}{\pi\delta^4} & 3D \\ \dfrac{3\Gamma(\psi_0)}{2\delta^3 B} & 2D \end{cases} \quad ; \quad \underline{w}_c\langle\boldsymbol{\xi}_{\mathbf{I}}^{i}\rangle = \begin{cases} \dfrac{4G_{ic}}{\pi\delta^4} & 3D \\ \dfrac{3G_{ic}}{2\delta^3 B} & 2D \end{cases} \tag{21}$$

where B is the thickness of the 2D model, $\Gamma(\psi_0)$ is the interfacial fracture toughness that is the function of mode mixity ψ_0, and G_{1c} ($i = 1$) and G_{2c} ($i = 2$) are the critical strain energy release rates of material 1 and 2, respectively.

As shown in Eq. (21), the value of $\underline{w}_c\langle\boldsymbol{\xi}\rangle$ is bond-dependent. For an interior bond $\boldsymbol{\xi}_{\mathbf{I}}^{i}$, it is uniform inside a material; while for an interface bond $\xi_{\mathbf{M}}$, it is the function of interfacial fracture toughness $\Gamma(\psi_0)$, in which the mode mixity ψ_0 can be obtained from Eq. (19). Since the value of ψ_0 of an interfacial crack may change with

loading condition and crack length, the value of $\underline{w}_c \langle \boldsymbol{\xi}_\mathbf{M} \rangle$ would also vary with the load situation and location of the interface bond.

Then, the MCED-based bond failure criterion can be expressed as:

$$\underline{d} \langle \boldsymbol{\xi} \rangle = \begin{cases} 1 & \text{if } \underline{w} \langle \boldsymbol{\xi} \rangle < \underline{w}_c \langle \boldsymbol{\xi} \rangle \text{ for all } t' \leq t, \\ 0 & \text{otherwise} \end{cases} \tag{22}$$

where $\underline{d} = 0$ means that the bond is irreversibly broken, the bond ξ can be an interface bond $\xi_\mathbf{M}$ or an interior bond $\boldsymbol{\xi}_\mathbf{I}^i (i = 1, 2)$ related to their corresponding values of $\underline{w}_c \langle \boldsymbol{\xi} \rangle$ in Eq. (21).

4.3. Path selection of an interface crack

For a bimaterial interface crack, it may propagate along the interface or kink out of the interface, depending on the loading condition and the fracture toughness of bimaterial interface and relative materials [3].

In above peridynamic bimaterial model, the bonds are divided into interface bonds $\xi_\mathbf{M}$ and interior bonds $\boldsymbol{\xi}_\mathbf{I}^i$ with their critical values $\underline{w}_c \langle \boldsymbol{\xi} \rangle$ in Eq. (21). As the MCED-based bond failure criterion in Eq. (22) is applied, there is a natural failure competition between interface bonds $\xi_\mathbf{M}$ and interior bonds $\boldsymbol{\xi}_\mathbf{I}^i$. When the bond energy densities $\underline{w} \langle \boldsymbol{\xi}_\mathbf{M} \rangle$ of interface bonds $\xi_\mathbf{M}$ successively arrive critical values $\underline{w}_c \langle \boldsymbol{\xi}_\mathbf{M} \rangle$, the interface crack will keep propagating along the interface with failure of interface bonds; while when the bond energy densities $\underline{w} \langle \boldsymbol{\xi}_\mathbf{I}^i \rangle$ of interior bonds $\boldsymbol{\xi}_\mathbf{I}^i$ near the crack tip arrive their $\underline{w}_c \langle \boldsymbol{\xi}_\mathbf{I}^i \rangle$, the interface crack will kink out the interface and grow inside the materials. The ratio of the MCED values between the interior bond $\boldsymbol{\xi}_\mathbf{I}^i$ and interface bond $\xi_\mathbf{M}$ is:

$$\chi_i = \frac{\underline{w}_c \langle \boldsymbol{\xi}_\mathbf{I}^i \rangle}{\underline{w}_c \langle \boldsymbol{\xi}_\mathbf{M} \rangle} = \frac{G_{ic}}{\Gamma (\psi_0)} \tag{23}$$

which naturally meets the classical interface crack kinking criterion in [3].

Thus, with the MCED-based bond failure model, the crack growth paths along or kinking out of the interface can be naturally captured with failure competition between interface bonds $\xi_\mathbf{M}$ and interior bonds $\boldsymbol{\xi}_\mathbf{I}^i$, and no extra fracture criterion is needed.

4.4. Progress of bimaterial interface fracture in peridynamics

The whole progress of peridynamics-based method for bimaterial interface fracture analysis is given in Fig. 9.

As shown in Fig. 9, the peridynamic scalar force state of Eq. (3) is applied for the elastic analysis of bimaterial system. For the bimaterial failure analysis, the bonds in peridynamic bimaterial model are identified as interface bonds $\xi_\mathbf{M}$ and interior bonds $\boldsymbol{\xi}_\mathbf{I}^i$ ($i = 1, 2$), which utilize the MCED-based failure model of Eq. (22) for bonds failure prediction. In the MCED model, the mode mixity ψ_0 of interface crack is timely computed by Eqs. (17)–(19), the interfacial fracture toughness is obtained from the function of $\Gamma (\psi_0)$, and the MCED values of the interface bond $\xi_\mathbf{M}$ and interior bond $\boldsymbol{\xi}_\mathbf{I}^i$ are obtained from Eq. (21).

In summary, a peridynamics-based frame is thus established for bimaterial interface fracture analysis. It can naturally be utilized for interface delamination analysis, and also path selection prediction of an interface crack.

5. Examples

In this section, four examples (i.e., a bimaterial plate under uniform tensile stress load, asymmetric bimaterial cantilever beams (ABCB) with an interface crack, a bimaterial single edge notched (BSEN) plate under tension or shear load and four-point shearing (FPS) test of rock–concrete bonded beam) are considered for verification and application of the peridynamic bimaterial elastic and fracture models.

5.1. A bimaterial plate under uniform tensile stress load

A bimaterial plate under uniform tensile stress load is first considered to validate the peridynamic bimaterial model for elastic analysis. The geometrical sizes of the plate are shown in Fig. 10, in which the plane stress and plane strain conditions are all considered, and the plate thickness B is 1 mm. The uniform tensile stress of 1 MPa
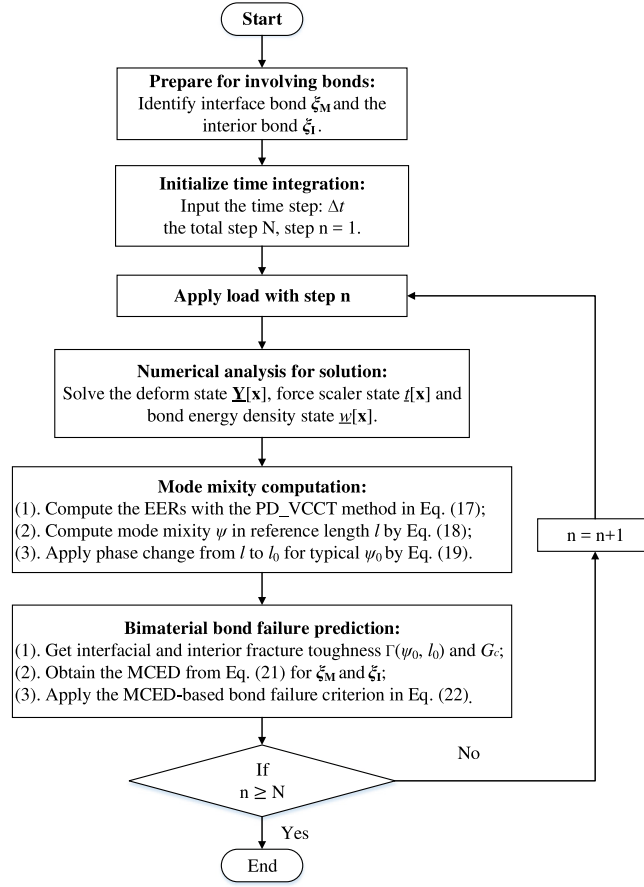
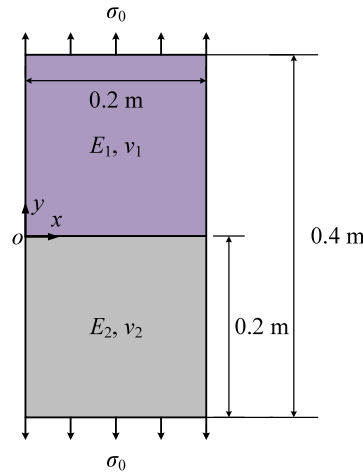**Fig. 9.** The whole progress of bimaterial interface fracture analysis in peridynamics.

Fig. 10. A bimaterial plate under uniform tensile stress load.

is applied as presented in Fig. 10. The elastic isotropic material 1 (E_1, v_1) and material 2 (E_2, v_2) are considered on the upper and lower sides of the interface, and material parameters take the values of $E_1 = 200$ GPa, $v_1 = 0.27$; $E_2 = 50$ GPa, $v_2 = 0.27$.
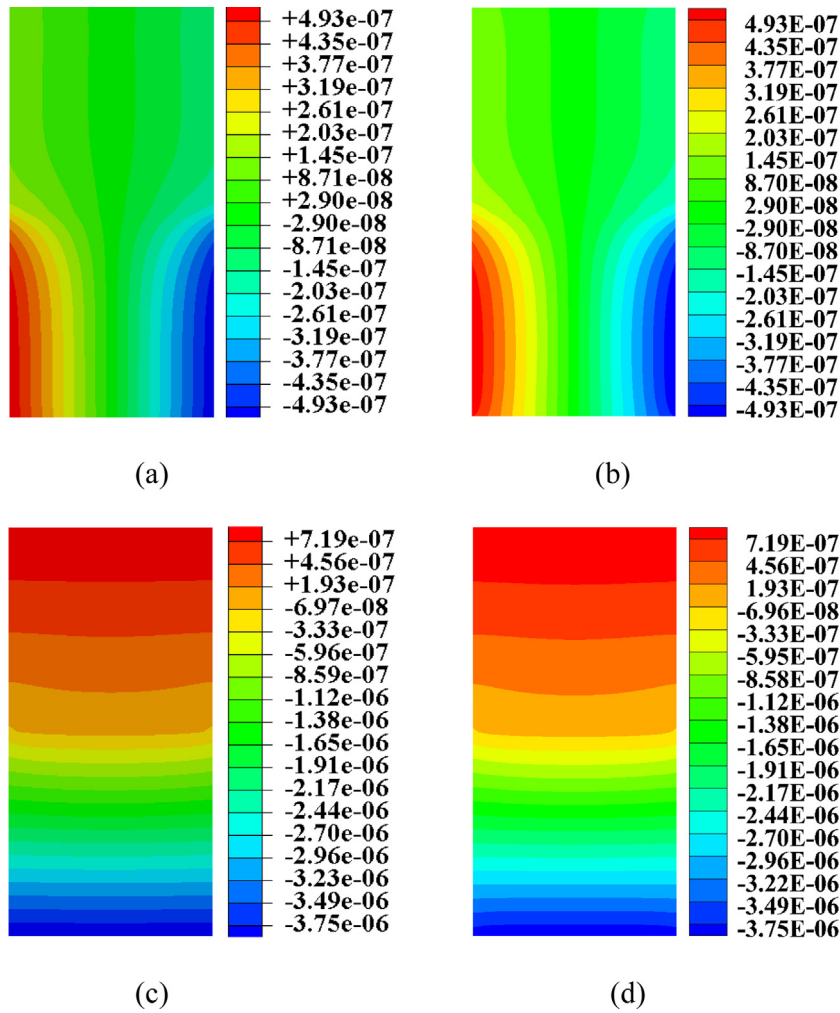
Fig. 11. Comparisons of displacement distributions in *x*-direction (m): (a) FEM and (b) Peridynamics, and *y*-direction: (c) FEM and (d) peridynamics, of the bimaterial plate in plane stress case.

In the numerical peridynamic model, uniform mesh size is used. The δ-convergence analysis [52] is performed with decreasing horizon values of $\delta = 8$ mm, 4 mm and 2 mm, and a fixed value of $m = 4$. The adaptive dynamic relaxation (ADR) method [53] is utilized for quasi-static analysis. The typical influence function of $\underline{\omega} = \delta/|\boldsymbol{\xi}|$ is utilized in this and following examples. The peridynamic scalar force state in Eq. (3) is performed for elastic behaviors prediction of this bimaterial plate and the numerical FEM analysis is also performed for the sake of comparison and validation.

Displacement distributions of the plate from the present peridynamic model and the FEM are given in Fig. 11, where fixed values of $\delta = 2$ mm and $m = 4$ with the plane stress condition are used. As shown in Fig. 11, the displacements from the present model greatly match those from the FEM solutions.

For the quantitative comparison, displacement components along the interface are presented in Fig. 12; while the *y*-direction displacement and volume dilatation (defined in Eq. (4)) along the middle of the bimaterial plate are presented in Figs. 13–14, where horizon values of $\delta = 8$ mm, 4 mm and 2 mm, and a fixed value of $m = 4$ are considered for the δ-convergence. Generally, it is shown that the results by proposed peridynamic bimaterial model are converging to the FEM solutions as nonlocal horizon δ decreases, in both the plane stress and plane strain cases. Typically, there is a great value drop of the volume dilatation in the bimaterial interface zone, and the disturbance
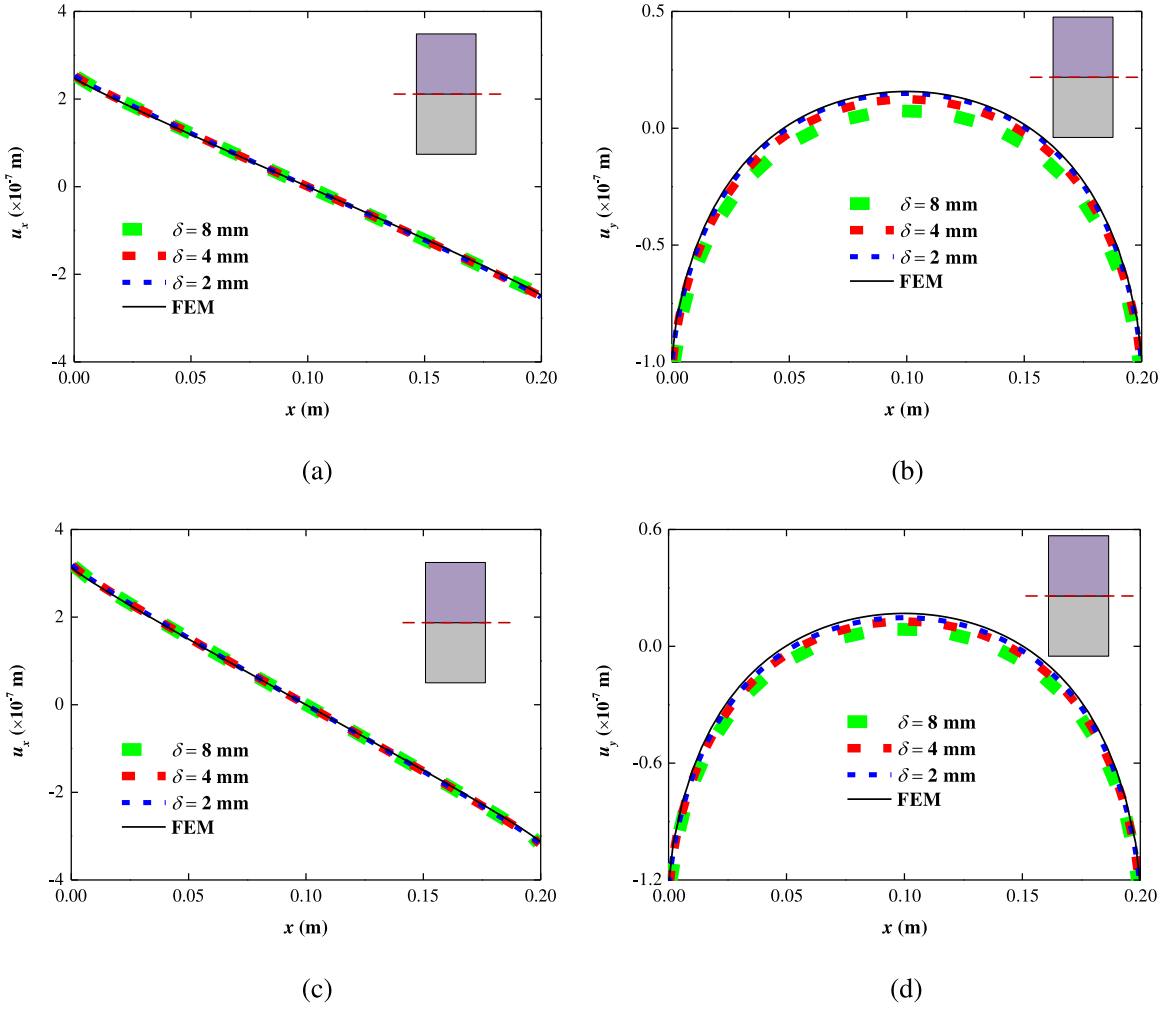
Fig. 12. Displacements along x-axis with different values of δ in the plane stress: (a) x component, and (b) y component, and plane strain cases: (c) x component, and (d) y component.

exists near the boundary (see Fig. 14), which meets the distribution of the equivalent nonlocal elastic modulus E' in Eq. (14).

5.2. Asymmetric bimaterial cantilever beams (ABCB) with an interface crack

The asymmetric bimaterial cantilever beam (ABCB) test (see Fig. 15) is then analyzed, in which geometrical sizes of the ABCB specimen are given as: $L = 160$ mm, $H_1 = 50$ mm and $H_2 = 30$ mm. A pre-crack a_0 exists along the bimaterial interface. And the plane strain condition is considered with the uniform beam thickness of $B = 1$ mm.

The elastic isotropic materials are used, in which $E_1 = 200$ GPa, $v_1 = 0.3$, $v_2 = 0.3$, and $E_2 = 200$ GPa and $E_2 = 100$ GPa are considered for bimaterial ratios of $E_1/E_2 = 1$ and $E_1/E_2 = 2$, respectively. For mixed-mode interface cracks, the interfacial fracture toughness is the function of the mode mixity. When $E_1/E_2 = 1$, the bimaterial mismatch vanishes, the Benzeggagh and Kenaue (B-K) law [54] can be applied as:

$$\Gamma(\psi_0) = G_{Ic} + (G_{IIc} - G_{Ic})\left(\frac{\psi_0^2}{\psi_0^2 + 1}\right)^{\eta} \tag{24}$$
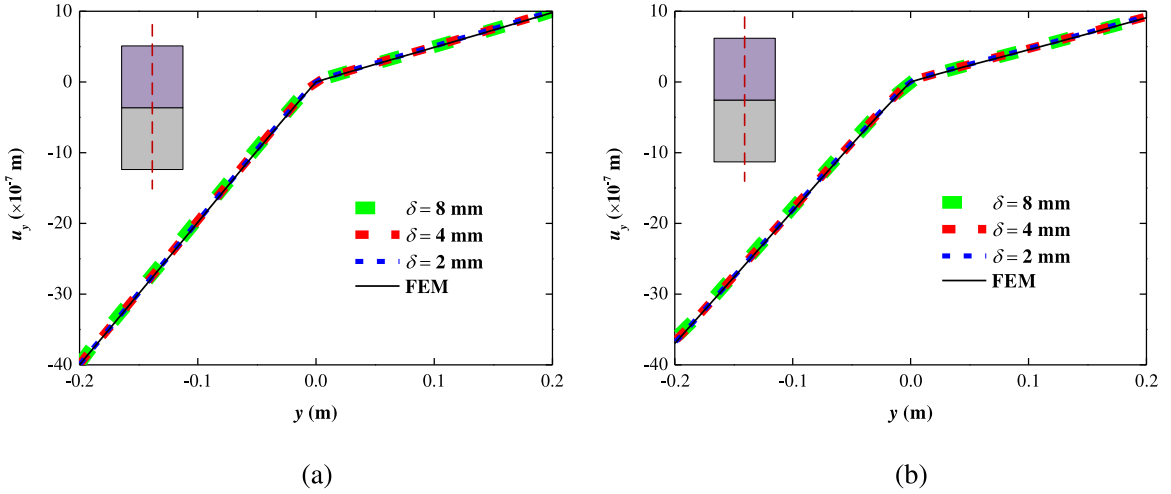
Fig. 13. The y-direction displacement along the line of $x = 100$ mm with different values of δ in the plane stress (a) and plane strain (b) cases.
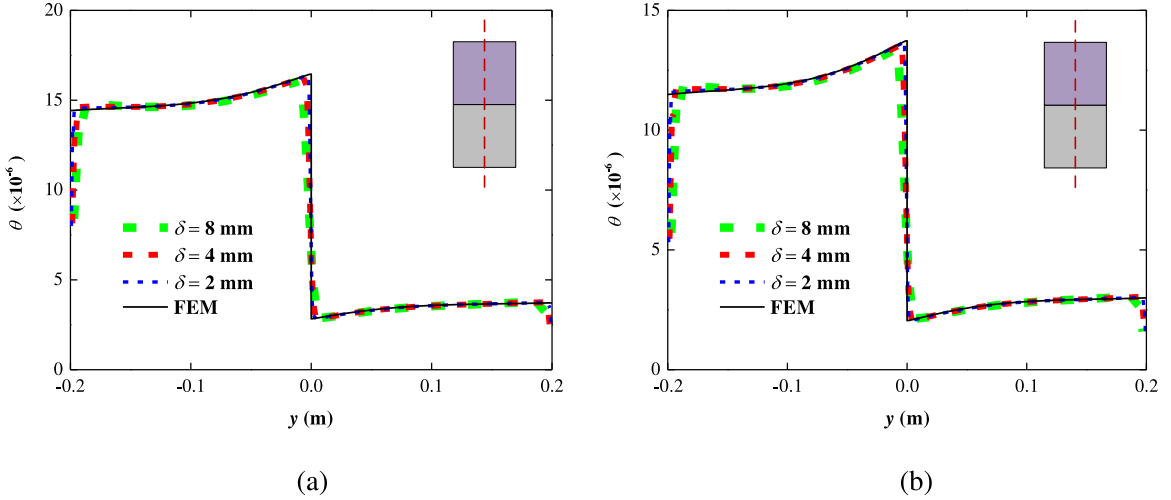

Fig. 14. The volume dilatation along the line of $x = 100$ mm with different values of δ in the plane stress (a) and plane strain (b) cases.

where $G_{I_c} = 30$ J/m^2, $G_{II_c} = 100$ J/m^2, η is equal 1 for simplification, and the mode mixity ψ_0 is equal to ERR-based mode mixity ψ_G computed from Eq. (18). While when $E_1/E_2 = 2$, the experimental interfacial fracture toughness function from Suo and Hutchinson [3] is considered as:

$$\Gamma(\psi_0) = G_c \left[1 + (1 - \lambda) \tan^2 \psi_0 \right] \tag{25}$$

where $G_c = 30$ J/m^2, λ is equal 0.3, and ψ_0 is the mesh-independent mode mixity in the typical reference length of $l_0 = 0.1$ mm, and it can be calculated by the phase change of Eq. (19) from the corrected mode mixity ψ.

In peridynamic numerical model, the δ-convergence [52] is performed with decreasing horizon values of $\delta = 4$ mm, 2 mm and 1 mm, and a fixed value of $m = 4$. And the progress in Fig. 9 is performed for bimaterial fracture analysis in peridynamics.

5.2.1. Elastic behaviors of the ABCB specimen

First, the fixed displacement load of $u_0 = -1.0 \times 10^{-4}$ m is applied in the ABCB specimen (see Fig. 15), and the pre-crack length $a_0 = 80$ mm is considered. For the ABCB specimen deformation analysis, the peridynamic
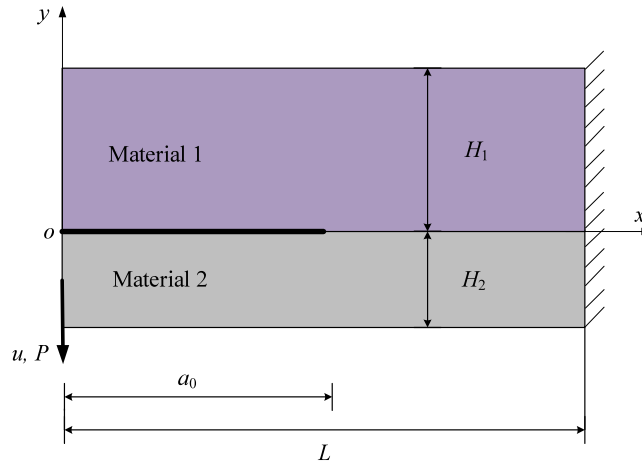
Fig. 15. Asymmetric bimaterial cantilever beams (ABCB) with an interface crack.

scalar force state in Eq. (3) is performed and the adaptive dynamic relaxation (ADR) method [53] is utilized for quasi-static elastic analysis.

The distributions of volume dilatation and strain energy density around the bimaterial interface crack tip are presented in Fig. 16, where bimaterial ratios of $E_1/E_2 = 1$ and $E_1/E_2 = 2$ are respectively considered. As shown in Fig. 16, the volume dilatation and strain energy density are concentrated at the crack tip with the asymmetric contour due to asymmetric loading, which reflects the mixed-mode state of the interface crack. And the contour mismatch exists near the bimaterial interface in case of $E_1/E_2 = 2$ because of the material parameter mismatch across the interface (see Fig. 16(b) and (d)).

Typically, the plots of volume dilatation along the line of $x = 82$ mm are presented in Fig. 17, where δ-convergence is performed and the FEM solutions are given for comparison. As shown in Fig. 17, the values of volume dilatation reach their maximum near the crack tip ($y = 0$ mm), and the plots from peridynamics converge to the FEM solutions as the value of δ decreases. Typically, in case of $E_1/E_2 = 2$, there is a much sharper drop of volume dilatation value across bimaterial interface, and the curves from peridynamics are smoother than the FEM solutions (see Fig. 17(b)), which show the smearing effect of peridynamic bimaterial model on elastic property presented in Fig. 5.

5.2.2. Energy release rates and mode mixity

The energy release rates (ERRs) and mode mixity of the ABCB specimens are computed with the fixed displacement load of $u_0 = -1.0 \times 10^{-4}$ m. The PD_VCCT-based method in Eqs. (17)–(19) is utilized, and the FEM solution is considered for comparison. When $E_1/E_2 = 2$, the mesh-independent mode mixity ψ is computed by the correction method in [7], in which the reference parameter $l = B$ (plate thickness) is used.

The ERRs and mode mixity of the ABCB specimens in cases of $E_1/E_2 = 1$ and $E_1/E_2 = 2$ are presented in Table 1 and Table 2, respectively, where the pre-crack length $a_0 = 80$ mm is considered with the δ-convergence. As shown in Table 1, when $E_1/E_2 = 1$, the values of ERRs and ERR-based mode mixity are mesh-independent. The results from presented peridynamic method converge to the FEM solutions as the value of δ decreases, and the maximum difference is 2%. When $E_1/E_2 = 2$ (see Table 2), the values of mode I and mode II ERRs and ERR-based mode mixity are mesh-dependent; while the total ERR and the corrected mode mixity ψ are mesh-independent, and the differences of the total ERR and ψ from the peridynamics to the FEM solutions are 0.89% and 2.82%, respectively.

Then, the total ERR and mode mixity ψ of the ABCB specimens for varying crack lengths from 40 mm to 120 mm are presented Figs. 18–19, where the mesh-independent correction method is performed for mode mixity ψ calculation in case of $E_1/E_2 = 2$. As shown in Figs. 18–19, both in $E_1/E_2 = 1$ and $E_1/E_2 = 2$ cases, the total ERR and ψ from the PD_VCCT have a good match with the FEM_VCCT solutions with the maximum difference of 3.1%.
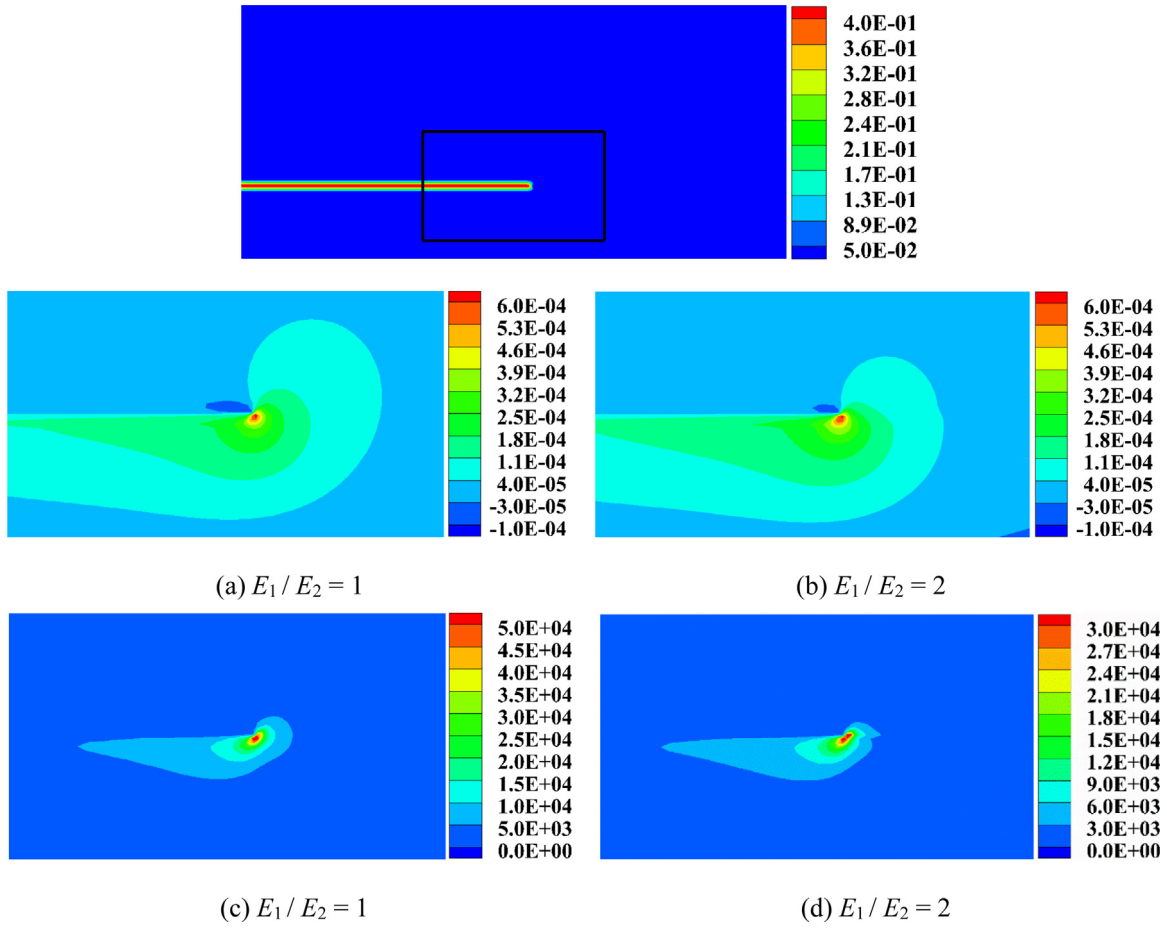
Fig. 16. Distributions of volume dilatation [(a) and (b)], strain energy density (J/m^3) [(c) and (d)] around interface crack tip of the ABCB specimens with $E_1/E_2 = 1$ and $E_1/E_2 = 2$ cases.
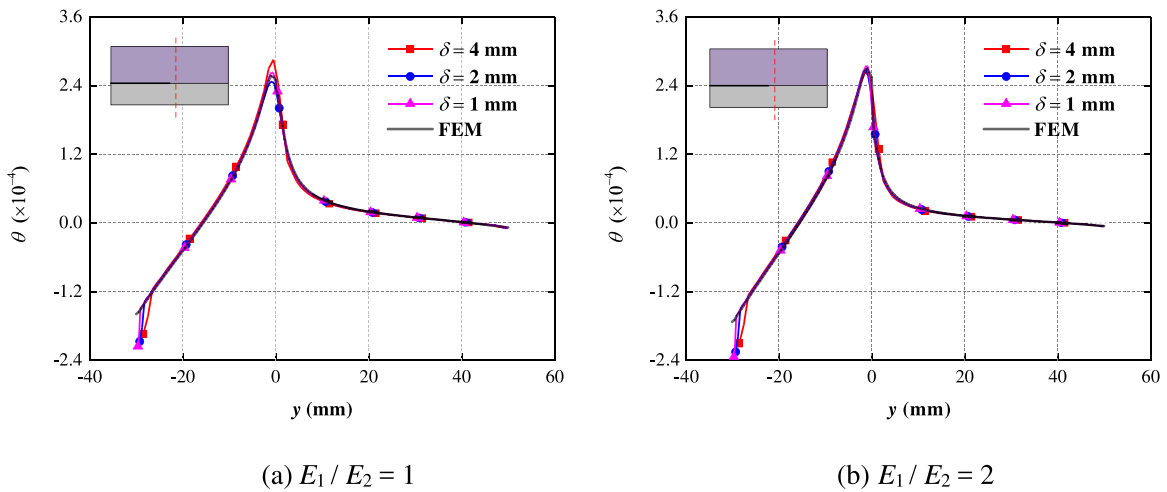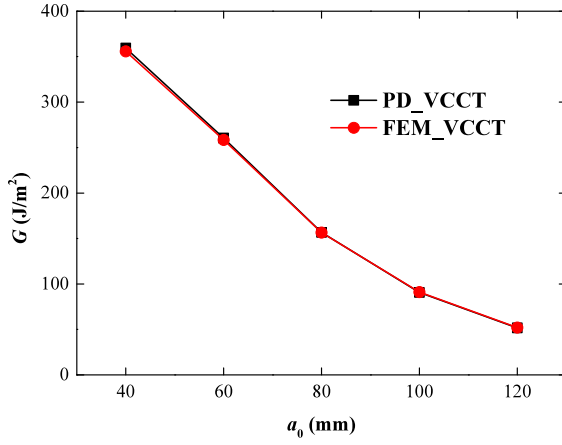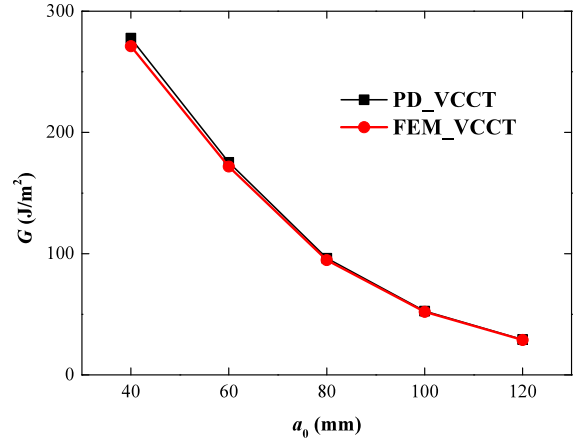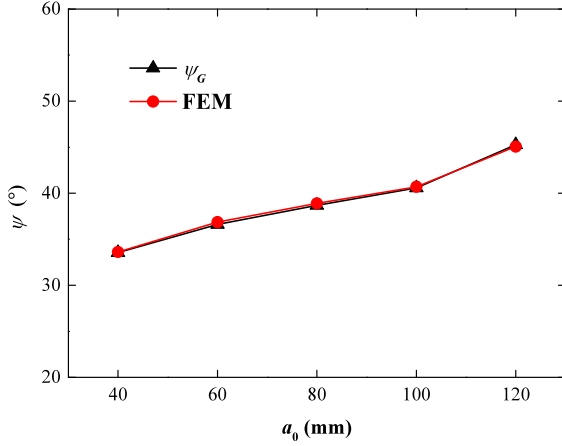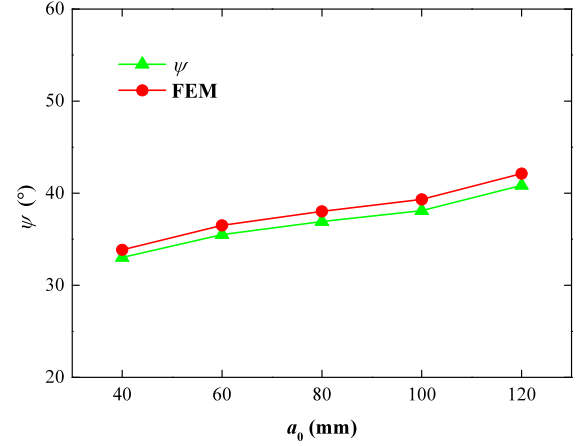

Fig. 17. Plots of volume dilatation along the line of $x = 82$ mm of the ABCB specimens with (a) $E_1/E_2 = 1$; (b) $E_1/E_2 = 2$.

(a) $E_1 / E_2 = 1$ (b) $E_1 / E_2 = 2$

Fig. 18. Total energy release rate of the ABCB specimens for varying values of crack length a_0: (a) $E_1/E_2 = 1$; (b) $E_1/E_2 = 2$.

(a) $E_1 / E_2 = 1$ (b) $E_1 / E_2 = 2$

Fig. 19. Mode mixity of the ABCB specimens for varying values of crack length a_0: (a) $E_1/E_2 = 1$; (b) $E_1/E_2 = 2$.

Table 1
Energy release rates and mode mixity when $E_1/E_2 = 1$.

Mesh size	G_I (J/m^2)	G_{II} (J/m^2)	ψ_G (°)
$\delta = 4$ mm	106.84	52.28	40.08
$\delta = 2$ mm	105.76	50.83	39.72
$\delta = 1$ mm	105.50	50.30	39.56
FEM ($\Delta x = 1$ mm)	107.10	49.37	38.90

5.2.3. Interface delamination of the ABCB specimen

The ABCB specimen is then applied with increasing displacement of $u(t) = -2.0 \times 10^{-2} * t$ m for interface delamination analysis. In the peridynamic numerical model, the explicit time integration is applied, and critical time steps for different mesh sizes are obtained from [16]. The proposed MCED-based failure model in Eq. (22) is utilized for bimaterial interface fracture analysis, in which interior bonds ξ_1^i are set as unbrokenable in this case

Table 2
Energy release rates and mode mixity when $E_1/E_2 = 2$.

Mesh size	G_I (J/m^2)	G_{II} (J/m^2)	G (J/m^2)	ψ_G (°)	ψ (°)
$\delta = 4$ mm	55.32	42.32	97.64	50.14	37.03
$\delta = 2$ mm	52.66	43.53	96.19	52.09	36.92
$\delta = 1$ mm	50.23	45.32	95.55	51.70	36.96
FEM ($\Delta x = 1$ mm)	52.00	42.70	94.70	51.92	38.03

for sake of interface delamination fracture. The interfacial fracture toughness functions in Eqs. (24) and (25) are considered for the cases of $E_1/E_2 = 1$ and $E_1/E_2 = 2$, respectively.

First, the fixed pre-crack length $a_0 = 80$ mm is considered, the distributions of y-direction displacement, strain energy density, crack path and released energy density of the ABCB specimen at crack propagation of 4×10^{-2} s and 10×10^{-2} s are presented in Fig. 20, where the bimaterial ratio of $E_1/E_2 = 2$ is considered. With the increasing y-directional displacement loading, the strain energy density is concentrated at the crack tip (see Fig. 20(c)), and the crack starts to grow from the location of pre-crack tip (see Fig. 20(e)) and propagates along the interface (see Fig. 20(f)). Meanwhile, the released energy density appears at pre-crack tip and follows with the crack path (see Fig. 20(g) and (h)). Typically, as shown in Fig. 20(h), the maximum value of the released energy density in fresh interfacial crack is larger than that of the behind crack, which reflects that the interfacial fracture toughness increases with the increasing crack mode mixity as interface crack growing (see Fig. 19).

The applied load–displacement plots of ABCB tests are shown in Fig. 21, where mesh sizes of $\delta = 4$ mm and 2 mm are considered. For comparison, when $E_1/E_2 = 1$, the FEM-based VCCT method with the same B-K interface law is performed for this ABCB test; while when $E_1/E_2 = 2$, the analytical deformation solution before the crack growth is considered. As shown in Fig. 21, the peridynamic model successfully captures the load–displacement relationship of the ABCB test as compared with the FEM-VCCT fracture and analytical deformation solutions.

Then, the ABCB specimens with varying crack lengths from 40 mm to 120 mm are investigated with the MCED-based bond failure criterion. The critical applied load P_c and displacement u_c for different values of pre-crack length a_0 are presented in Fig. 22, in which the material ratio of $E_1/E_2 = 2$ is considered. And for comparison, the ERR-based analytical solutions of critical load and displacement can be obtained as:

$$P_c = P\sqrt{\frac{\Gamma(\psi_0)}{G(a)}}, \ u_c = u_0\sqrt{\frac{\Gamma(\psi_0)}{G(a)}} \tag{26}$$

where $u_0 = -1.0 \times 10^{-4}$ m is the fixed displacement load, P is the applied load of the ABCB specimen for pre-crack length a_0, $G(a)$ is the total energy release rate that given in Fig. 18(b), and $\Gamma(\psi_0)$ is the experimental interfacial fracture toughness in Eq. (25). As shown in Fig. 22, the critical load and displacement from the peridynamic model greatly match those from the ERR-based analytical solutions, and the differences of PD predicted critical load and displacement to ERR-based results are 4.97% and 4.90%, respectively.

5.2.4. Growth path competition of the ABCB interface crack

Last, different ratios $\chi_2 = G_{2c}/\Gamma(\psi_0)$ of material 2 critical energy release rate to interfacial fracture toughness are considered, and the crack path competition between interface delamination and interface crack kinking is investigated.

The distribution of local damage (crack path) and released energy density of the ABCB specimen in case of $E_1/E_2 = 2$ are given in Fig. 23, where the pre-crack length of $a_0 = 80$ mm is considered, and different ratios of $\chi_2 = 1, 2$ and 4 are respectively considered. As shown in Fig. 23, when $\chi_2 = 1$, the interface crack directly kinks into material 2 as the increasing displacement is applied; when $\chi_2 = 4$, the crack keeps growing along the bimaterial interface; while when $\chi_2 = 2$, the crack firstly grows along the bimaterial interface and then kinks into material 2 in the approximate location of $x = 110$ mm. It is because when the crack grows along the interface, the value of $\Gamma(\psi_0)$ increases with the increasing of the mode mixity (see Fig. 19), which leads to the value decreasing of χ_2. According to numerical tests with different χ_2, the critical value of χ_{2c} for this interface crack kinking is 1.8, which means that if the input value $\chi_2 < 1.8$, the interface crack will start to grow by kinking into material 2; while if $\chi_2 > 1.8$, the interface crack will grow along the interface at the initiation time.
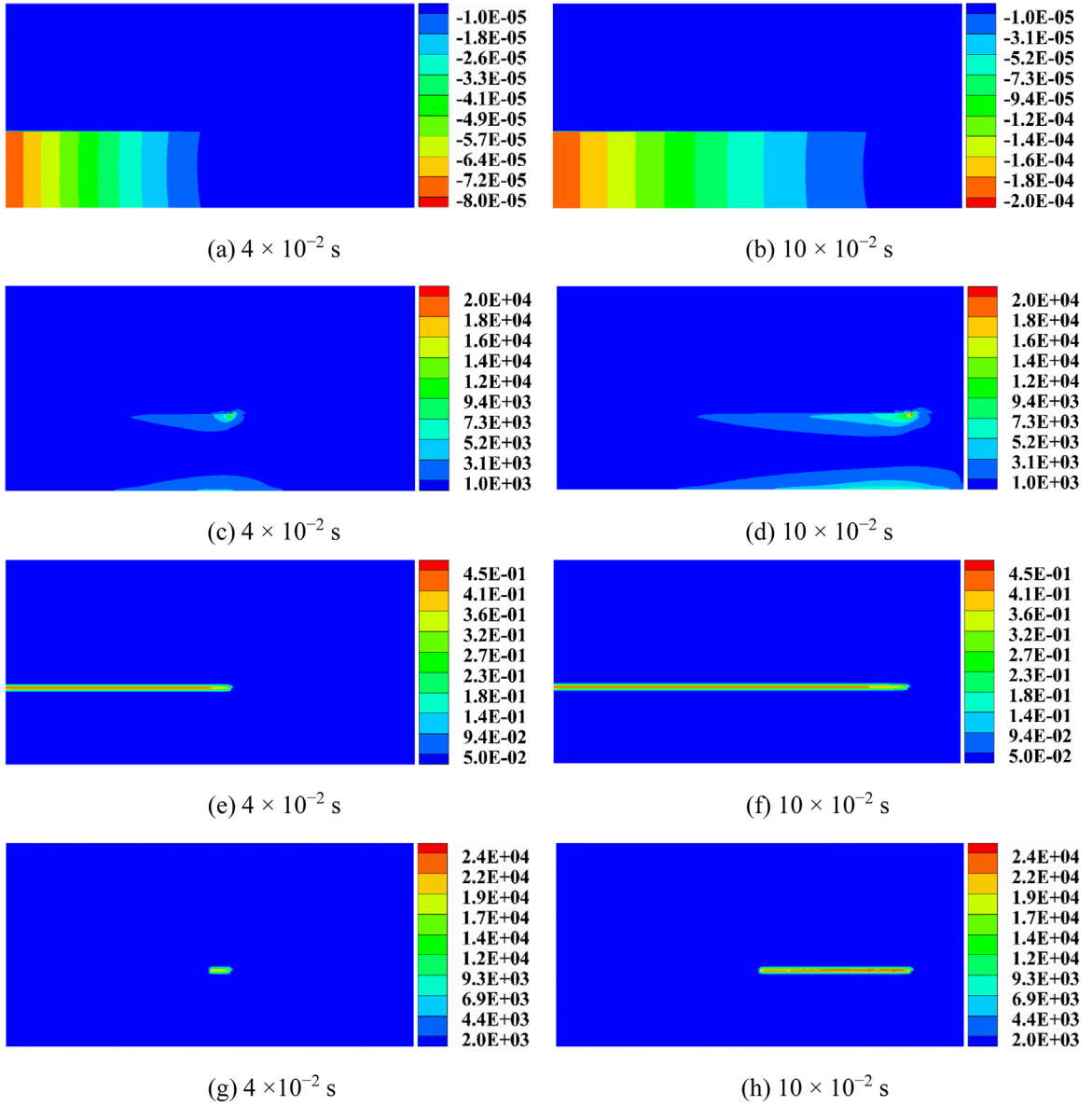
Fig. 20. Distributions of y-direction displacement (m) [(a) and (b)], strain energy density (J/m^3) [(c) and (d)], local damage/crack propagation [(e) and (f)], and released energy density (J/m^3) [(g) and (h)] of the ABCB specimen ($E_1/E_2 = 2$) at crack propagation of 4×10^{-2} s and 10×10^{-2} s.

In summary, the elastic and fracture behaviors of the ABCB specimen are successfully captured with the proposed peridynamics-based method, the energy release rates and mode mixity are computed, and the interface delamination fracture and crack path selection are well predicted.

5.3. A bimaterial single edge notched (BSEN) plate under tension or shear load

The geometrical sizes and boundary conditions of the bimaterial single edge notched (BSEN) plate are presented in Fig. 24, where the tension and shear load are respectively considered. The plane strain condition is performed, and the uniform beam thickness of $B = 1$ mm is used. A pre-crack along the interface of $a_0 = 50$ mm is considered. The elastic isotropic materials are utilized, in which $E_1 = 90$ GPa, $v_1 = 0.3$, $v_2 = 0.3$, and $E_2 = 90$ GPa and

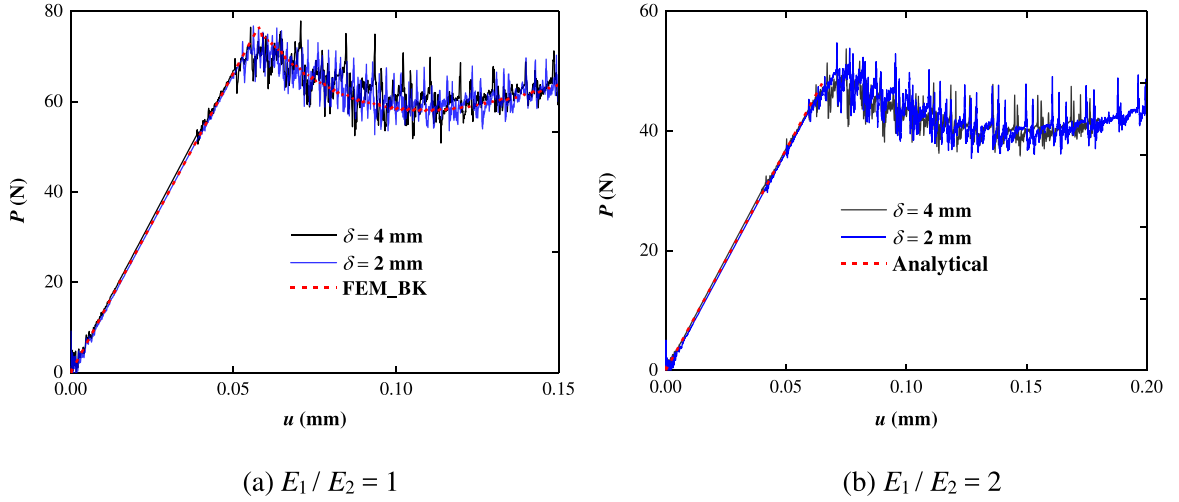(a) $E_1 / E_2 = 1$ (b) $E_1 / E_2 = 2$

Fig. 21. Applied load versus displacement of ABCB specimens by the peridynamic MCED model with comparisons to FEM and analytical solutions: (a) $E_1/E_2 = 1$; (b) $E_1/E_2 = 2$.
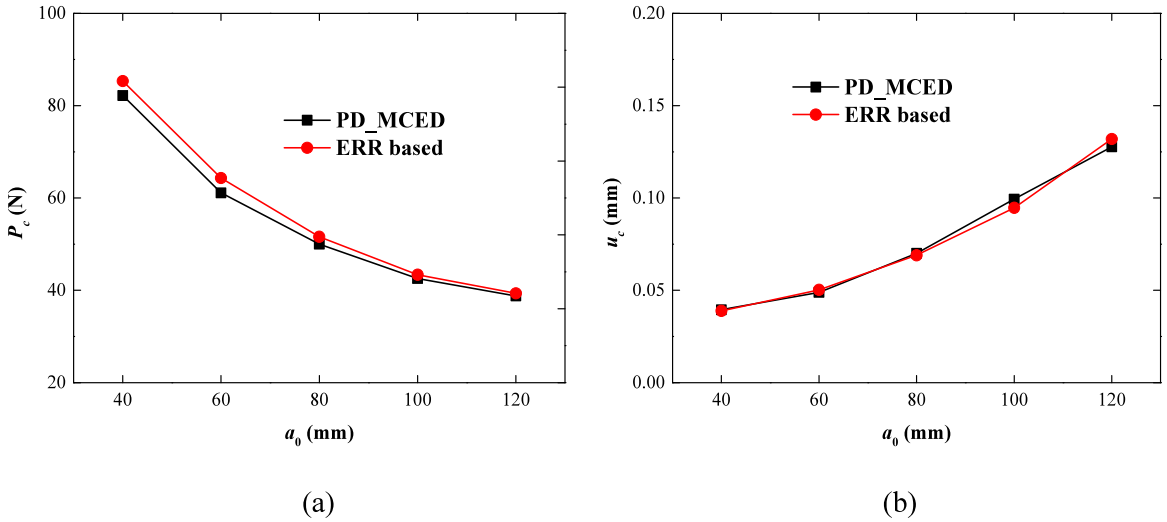

(a)   (b)

Fig. 22. The critical applied load (a), and critical displacement (b) of bimaterial specimens for varying values of crack length a_0 in case of $E_1/E_2 = 2$.

$E_2 = 9$ GPa are used for bimaterial ratios of $E_1/E_2 = 1$ and $E_1/E_2 = 10$. The interfacial fracture toughness function in Eq. (25) is also utilized in this example. And for peridynamic modeling, the fixed value of $m = 4$ is used, and different values of $\delta = 4$ mm and 2 mm are considered. The peridynamic elastic model in Eq. (3) is performed for deformation prediction, and the progress in Fig. 9 is performed for fracture analysis in peridynamics.

First, the fixed loads of tension displacement $u_1 = 1.0 \times 10^{-2}$ mm or shear displacement $u_2 = 1.0 \times 10^{-2}$ mm are respectively applied in the BSEN plate (see Fig. 24). The adaptive dynamic relaxation (ADR) method [53] is utilized for quasi-static elastic analysis. The PD_VCCT-based method in Eqs. (17)–(19) is performed for total energy release rate (ERR) and mode mixity computations, in which the mesh-independent mode mixity ψ is obtained by the correction method with the reference parameter of $l = B$ in case of $E_1/E_2 = 10$. And the FEM-based VCCT method is also performed for ERR computation. Thus, the values of total ERR and mode mixity of the BSEN plate under the tension or shear load are reported in Table 3. As shown in Table 3, when the tension load is applied, the interface crack of the BSEN plate is nearly in the pure mode I condition for both $E_1/E_2 = 1$ and $E_1/E_2 = 10$ cases;
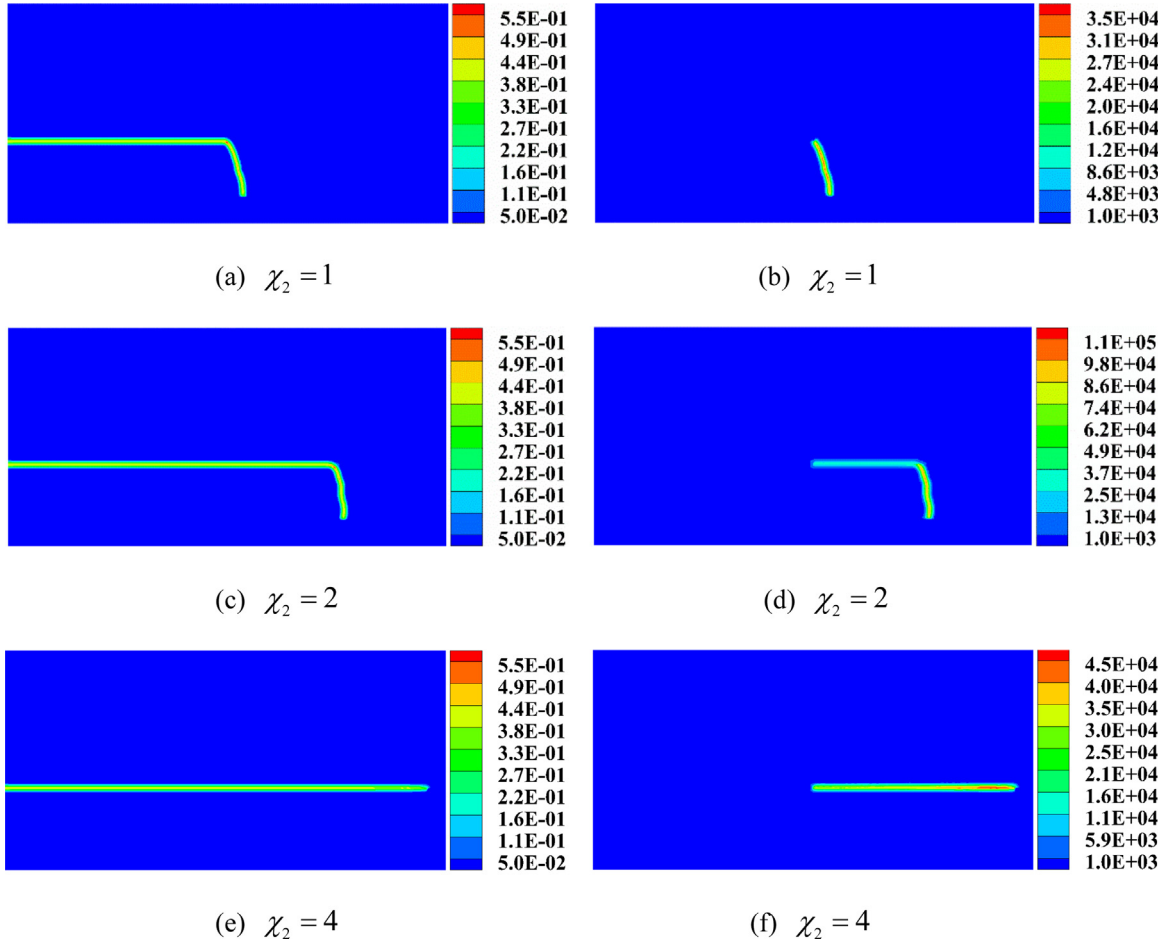
Fig. 23. The distribution of local damage [(a), (c) and (e)], and released energy density (J/m^3) [(b), (d) and (f)] of the ABCB specimens ($E_1/E_2 = 2$) for varying fracture toughness ratios of χ_2.
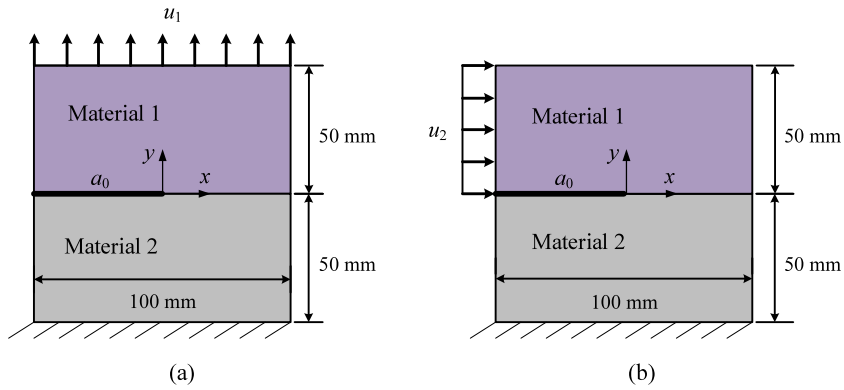

Fig. 24. The bimaterial single edge notched (BSEN) specimen under (a) tension or (b) shear load.

while when the shear load is applied, the interface crack is under mode II dominated condition, and the mode mixity of interface cracks in case of $E_1/E_2 = 10$ is larger than that in $E_1/E_2 = 1$ case. Typically, the predicted values of total ERR from the PD_VCCT method greatly match the FEM solutions, which are 52.09 J/m^2 ($E_1/E_2 = 1$), 10.41 J/m^2

(a) 7.2×10^{-3} mm   (b) 8.4×10^{-3} mm

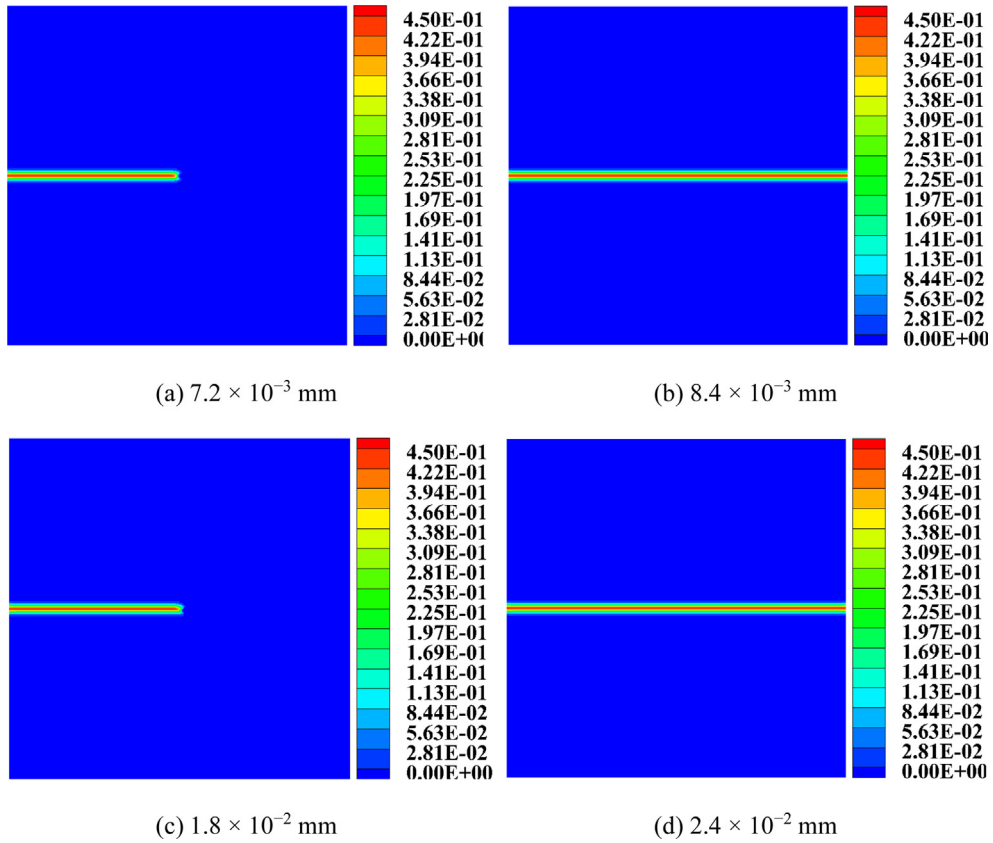(c) 1.8×10^{-2} mm   (d) 2.4×10^{-2} mm

Fig. 25. The local damage of the BSEN specimens under typical tensile displacement loads in cases of $E_1/E_2 = 1$ [(a) and (b)], and $E_1/E_2 = 10$ [(c) and (d)].
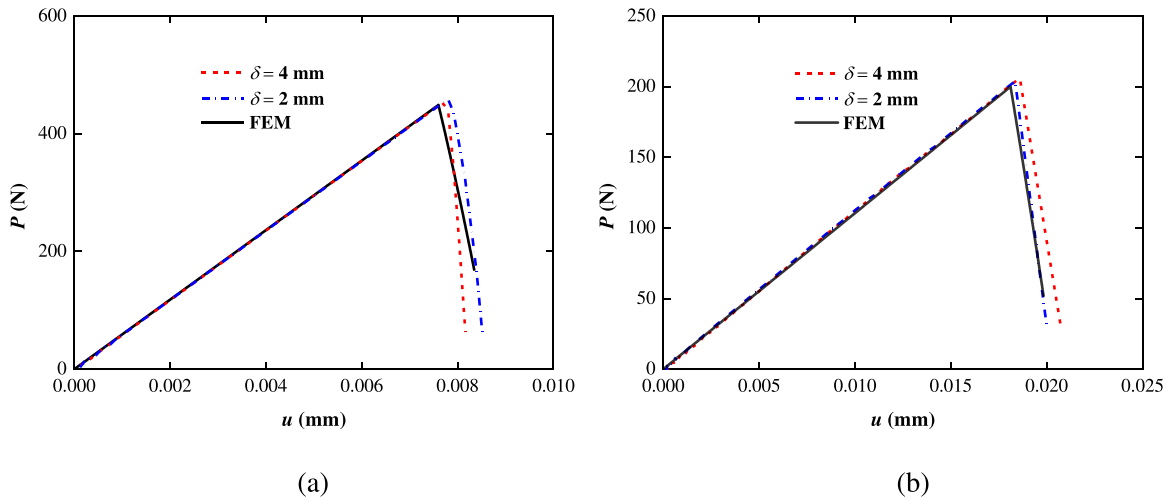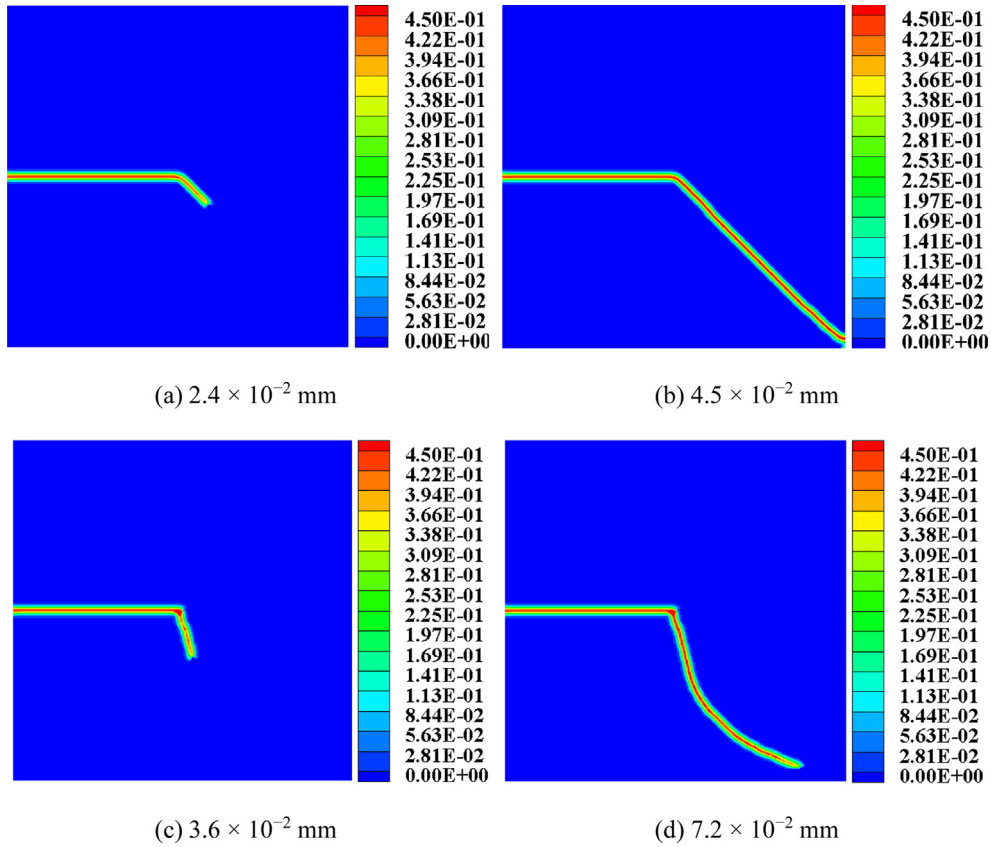

(a)   (b)

Fig. 26. Applied load versus displacement of the BSEN specimens under tension loading: (a) $E_1/E_2 = 1$; (b) $E_1/E_2 = 10$.

Fig. 27. The local damage of the BSEN specimens under typical shear displacement loads in cases of $E_1/E_2 = 1$ [(a) and (b)], and $E_1/E_2 = 10$ [(c) and (d)].

$(E_1/E_2 = 10)$ and 14.22 J/m^2($E_1/E_2 = 1$), 1.87 J/m^2 $(E_1/E_2 = 10)$ for tension and shear loads, respectively. And the maximum difference of the total ERR from the peridynamics to the FEM solutions is 3.0%.

Using the values of the mode mixity in Table 3, and considering the interfacial fracture toughness function of Eq. (25), the corresponding interfacial fracture toughness $\Gamma(\psi_0)$ for different load conditions and bimaterial ratios can be obtained. When tension load is considered, $\Gamma(\psi_0)$ is equal to 30 J/m^2 and 32.23 J/m^2 for $E_1/E_2 = 1$ and $E_1/E_2 = 10$ cases; while in the shear load condition, $\Gamma(\psi_0)$ is equal to 91.05 J/m^2 and 262.21 J/m^2 for the cases of $E_1/E_2 = 1$ and $E_1/E_2 = 10$, respectively. And in the following fracture analysis, the material 2 critical energy release rate is set as 30 J/m^2 for simplification.

Then, the BSEN plate is applied with linearly increasing tensile displacement load. The local damage (crack path) of BSEN plates with increasing displacement tensile loading are presented in Fig. 25, where bimaterial ratios of $E_1/E_2 = 1$ and $E_1/E_2 = 10$ are respectively analyzed. As shown in Fig. 25, with the increasing tensile displacement loading, the crack starts to grow and propagates rapidly along the interface (see Fig. 25(b) and (d)). Additionally, the applied load–displacement curves of BSEN tension tests are given in Fig. 26, where mesh sizes of $\delta = 4$ mm and 2 mm are respectively used, and the FEM solutions are also given for comparison. As shown in Fig. 26, for both $E_1/E_2 = 1$ and $E_1/E_2 = 10$ cases, the applied loads linearly increase with the displacement, and drop suddenly when the cracks start to grow. And the predicted curves from the peridynamic model greatly match those from the FEM results.

In the BSEN shear test, the linearly increasing shear displacement load is considered, and the crack paths of BSEN plates are presented in Fig. 27. As shown in Fig. 27, the cracks start to grow by kinking into material 2 (see Fig. 27(a) and (c)), and the kinking angle in case of $E_1/E_2 = 10$ is larger than that of $E_1/E_2 = 1$ case, since the crack mode mixity is larger when $E_1/E_2 = 10$. In addition, the applied load–displacement plots of BSEN shear tests
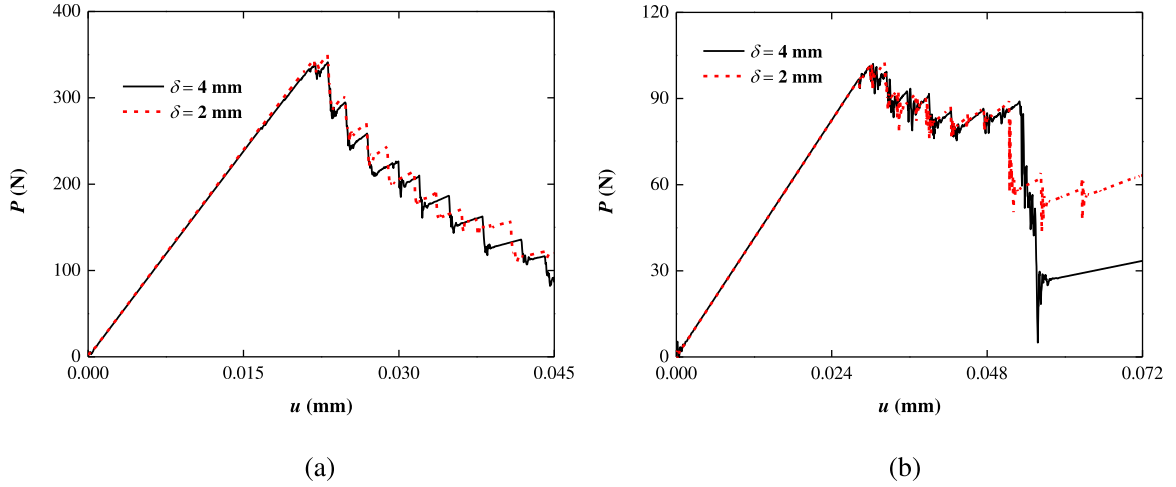
Fig. 28. Applied load versus displacement of the BSEN specimens under shear loading: (a) $E_1/E_2 = 1$; (b) $E_1/E_2 = 10$.

Table 3
Simulation results of BSEN plate under tension or shear loads.

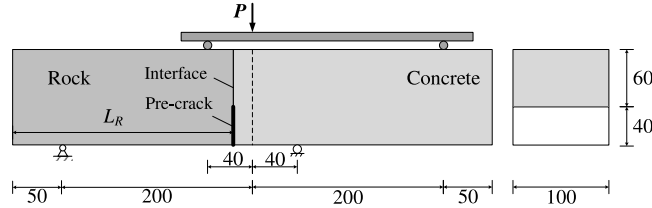| E_1 / E_2	Tension load		Shear load	
	1	10	1	10
G (J/m^2)	50.88	10.41	14.27	1.87
ψ (°)	0.65	5.26	59.61	70.23

Fig. 29. Four-point shearing (FPS) test of rock–concrete bonded specimen (mm).

are presented in Fig. 28. Compared to the BSEN tension test, the crack propagation process of the shear test lasts for a longer time with the increasing displacement load, and the numerical disturbance exists when cracks start to grow because of the explicit integration strategy.

Thus, for the BSEN tension test, though the material mismatch leads to the mode mixity in crack tip, the mode mixity has small effect on the interface delamination fracture. While for the BSEN shear test, the material mismatch across the interface has a great effect on crack mode mixity as well as the kinking angle.

5.4. Four-point shearing (FPS) test of rock–concrete bonded beam

The fracture characteristics of rock–concrete interface were experimental studied by the four-point shearing (FPS) test in [55]. In this section, this FPS specimen is analyzed with the proposed peridynamic bimaterial models.

The rock–concrete bonded beam under the FPS condition is given in Fig. 29, in which the pre-crack along the interface is considered with the length 40 mm. The interface crack is under the mixed mode condition, and a wide range of mode mixity ratio ψ can be obtained when the values of rock section length L_R are ranging from 210 mm to 250 mm. The material properties of the rock and concrete are reported in Table 4. And the interface fracture toughness of the rock–concrete interface obtained from the experimental data is [55]:
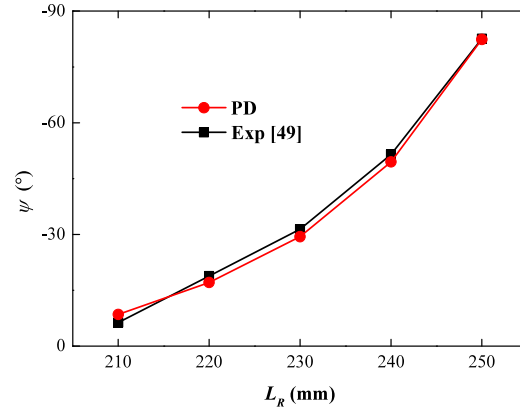
$$\Gamma(\psi_0) = 17.4 \left[1 + \tan^2(0.56\psi_0) \right] \tag{27}$$

Fig. 30. Mode mixity of the FPS specimens for varying values of rock length L_R.

(a) L_R = 210 mm   (b) L_R = 220 mm

(c) L_R = 230 mm

(d) L_R = 240 mm
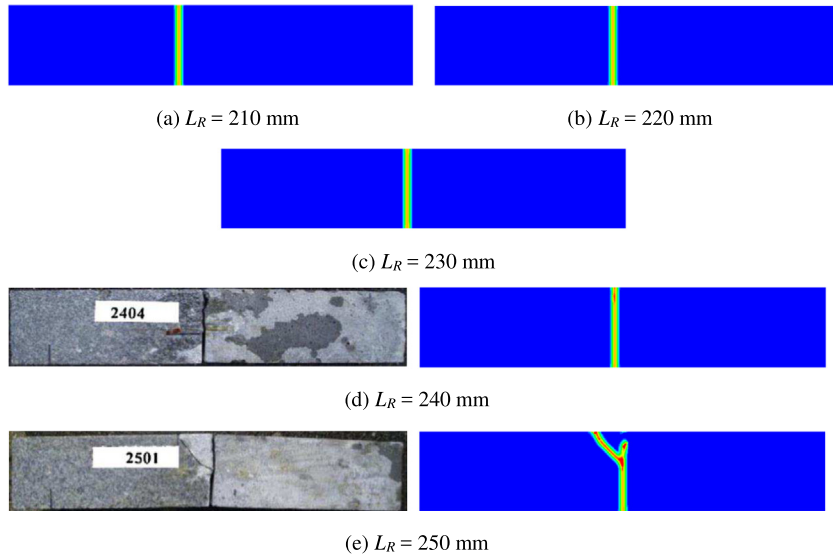
(e) L_R = 250 mm

Fig. 31. Crack paths of FPS specimens with different rock length L_R, with comparisons to the experimental results in [(d) and (e)].

For the peridynamic modeling, the plane strain condition is considered, and the uniform beam thickness of $B = 100$ mm is used. The fixed mesh sizes of $\delta = 8$ mm and $m = 4$ are considered. The linearly increasing force load P is applied, in which the ratio of force loads on the two loading points is 1:5 (see Fig. 29). The proposed progress in Fig. 9 is utilized for this rock–concrete interface fracture analysis.

The mode mixity of FPS specimens for varying values of rock length L_R is presented in Fig. 30, in which the peridynamics-based method in Eqs. (17)–(19) is performed. As shown in Fig. 30, the values of interface crack mode mixity are significantly increasing with the rock length L_R, and the rock–concrete interface cracks are gradually changing from mode I-dominated condition to mode-II dominated condition as L_R increases from 210 mm to 250 mm. Meanwhile, the values of mode mixity predicted from peridynamic model greatly match the data from the experiment in [55].

The local damage (crack path) of FPS specimens with varying rock length L_R are presented in Fig. 31, in which experimental results from [55] are given in cases of $L_R = 240$ mm and 250 mm. As shown in Fig. 31, same as the experimental result, when $L_R \leq 240$ mm, the cracks grow along the rock–concrete interface; while when $L_R = 250$ mm, the interface crack grows by kinking into rock and propagates toward the loading location. It is because when rock length L_R is approaching 250 mm, the mode mixity increases rapidly (see Fig. 30), the interface
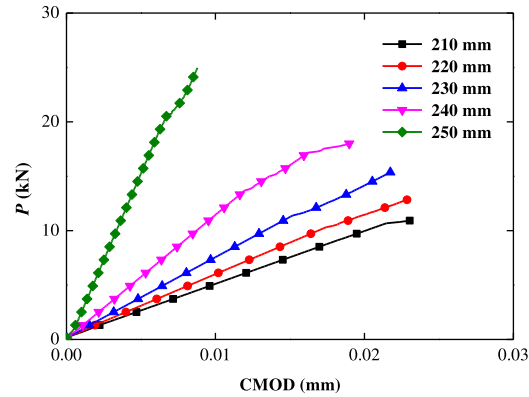
Fig. 32. Applied load-crack mouth opening displacement (P-CMOD) curves of the FPS specimens for varying values of rock length L_R.
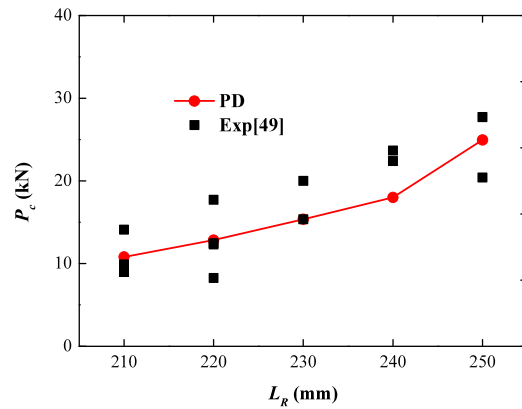

Fig. 33. Critical applied loads of the FPS specimens for varying values of rock length L_R: proposed peridynamic model (PD) and the experimental data (Exp).

Table 4
Material properties of rock and concrete [55].

Material	E (GPa)	v	ρ (kg/m^3)	G_c (J/m^2)
Rock	18.10	0.323	2750	51.2
Concrete	27.85	0.178	2350	71.0

fracture toughness obtained from Eq. (27) reaches its maximum value, and the interface crack prefers to kink into the rock material based on the crack path competition of Eq. (23).

Meanwhile, applied load related to crack mouth opening displacement (P-CMOD) curves of the FPS tests are presented in Fig. 32, where the CMOD is obtained from the relative displacement of the two-sided points of the interface crack mouth. As shown in Fig. 32, for all L_R, the applied loads P nearly increase linearly with the CMOD, and reach their critical values when cracks start to grow. And for the larger rock length L_R, the slopes of curves are relatively higher because of their larger mode mixity ratio. Additionally, the critical applied loads P_c of FPS tests for different values of rock length L_R are shown in Fig. 33, where the experimental data from [55] are considered for comparison. As presented in Fig. 33, the critical applied load predicted from the peridynamic model have a reasonable agreement with the experiment data.

6. Conclusions

In this paper, the peridynamics-based models are proposed for the bimaterial interface fracture investigation. First, the nonlocal bimaterial interface model for interior force transferring is presented, and the MCED-based bond

failure model is proposed for interface crack analysis. Then, four examples of a bimaterial plate under uniform tensile stress load, asymmetric bimaterial cantilever beams (ABCB), bimaterial single edge notched (BSEN) and four-point shearing (FPS) tests, are analyzed for the model verification and application.

In the ABCB test, the peridynamics-based model can well capture the elastic and fracture behaviors of the ABCB specimens, in which the interface delamination fracture and crack path selection are well predicted. The energy release rates and mode mixity computed from peridynamics greatly match those from FEM solutions within the difference of 3.1%, and the predicted critical load and displacement values are within the difference of 5.0% to ERR-based results. While in the BSEN and FPS tests, under mode-I dominated condition, the interface cracks grow along the interface crack; while in mode-II dominated condition, the interface cracks prefer to grow by kinking into materials. And the material mismatch and loading condition have a great effect on the crack mode mixity and kinking angle.

In conclusion, the proposed peridynamics-based method can successfully capture the characteristics of bimaterial interface fracture. With capability of this proposed model on bimaterial fracture, the peridynamic theory can be further extended for failure analysis of layered structure and adhesive joints.

Declaration of competing interest

The authors declare that they have no known competing financial interests or personal relationships that could have appeared to influence the work reported in this paper.

Acknowledgments

References

[1] J.R. Rice, G.C. Sih, Plane problems of cracks in dissimilar media, J. Appl. Mech. 32 (1965) 418–423.

[2] M.L. Williams, The stresses around a fault or a crack in dissimilar media, Bull. Seismol. Soc. Am. 49 (1959) 199–204.

[3] J.W. Hutchinson, Z.G. Suo, Mixed mode cracking in layered materials, Adv. Appl. Mech. 29 (1992) 63–191.

[4] R. Yuuki, J. Liu, J. Xu, T. Ohira, T. Ono, Mixed mode fracture criteria for an interface crack, Eng. Fract. Mech. 47 (1994) 367–377.

[5] M. He, J.W. Hutchinson, Kinking of a crack out of an interface, J. Appl. Mech. 56 (1989) 270–278.

[6] R.L. Williamson, B.H. Rabin, J.T. Drake, Finite element analysis of thermal residual stresses at graded ceramic–metal interfaces. Part I. Model description and geometrical effects, J. Appl. Phys. 74 (1993) 1310–1320.

[7] A. Agrawal, A.M. Karlsson, Obtaining mode mixity for a bimaterial interface crack using the virtual crack closure technique, Int. J. Fract. 141 (2006) 75–98.

[8] Y. Freed, L. Banks-sills, A new cohesive zone model for mixed mode interface fracture in bimaterials, Eng. Fract. Mech. 75 (2008) 4583–4593.

[9] Z. Jin, C.T. Sun, Cohesive zone modeling of interface fracture in elastic bi-materials, Eng. Fract. Mech. 72 (2005) 1805–1817.

[10] T. Belytschko, T. Black, Elastic crack growth in finite elements with minimal remeshing, Internat. J. Numer. Methods Engrg. 45 (1999) 601–620.

[11] S.A. Silling, Reformulation of elasticity theory for discontinuities and long-range forces, J. Mech. Phys. Solids. 48 (2000) 175–209.

[12] S.A. Silling, E. Askari, A meshfree method based on the peridynamic model of solid mechanics, Comput. Struct. 83 (2005) 1526–1535.

[13] Q. Zhu, T. Ni, Peridynamic formulations enriched with bond rotation effects, Internat. J. Engrg. Sci. 121 (2017) 118–129.

[14] Y. Wang, X. Zhou, Y. Wang, Y. Shou, A 3-D conjugated bond-pair-based peridynamic formulation for initiation and propagation of cracks in brittle solids, Int. J. Solids Struct. 134 (2018) 89–115.

[15] S.A. Silling, M. Epton, O. Weckner, J. Xu, E. Askari, Peridynamic states and constitutive modeling, J. Elasticity 88 (2007) 151–184.

[16] H. Zhang, P. Qiao, A two-dimensional ordinary state-based peridynamic model for elastic and fracture analysis, Eng. Fract. Mech. 232 (2020) 107040.

[17] X. Gu, E. Madenci, Q. Zhang, Revisit of non-ordinary state-based peridynamics, Eng. Fract. Mech. 190 (2018) 31–52.

[18] J.A. Mitchell, A nonlocal, ordinary, state-based plasticity model for peridynamics, Albuquerque SAND, 2011, pp. 2011–3166.

[19] E. Madenci, S. Oterkus, Ordinary state-based peridynamics for plastic deformation according to von mises yield criteria with isotropic hardening, J. Mech. Phys. Solids. 86 (2016) 192–219.

[20] J.A. Mitchell, A. non local, Ordinary state-based viscoelasticity model for peridynamics, Albuquerque SAND, 2011, pp. 2011–8064.

[21] J.T. Foster, S.A. Silling, W.W. Chen, Viscoplasticity using peridynamics, Internat. J. Numer. Methods Engrg. 81 (2009) 1242–1258.

[22] H. Zhang, P. Qiao, A state-based peridynamic model for quantitative fracture analysis, Int. J. Fract. 211 (2018) 217–235.

[23] J.T. Foster, S.A. Silling, W. Chen, An energy based failure criterion for use with peridynamic states, Int. J. Multiscale Comput. Eng. 9 (2011) 675–687.

[24] Y. Zhang, P. Qiao, A new bond failure criterion for ordinary state-based peridynamic mode II fracture analysis, Int. J. Fract. 215 (2019) 105–128.

[25] H. Zhang, X. Zhang, P. Qiao, A new peridynamic mixed-mode bond failure model for interface delamination and homogeneous materials fracture analysis, Comput. Methods Appl. Mech. Engrg. 379 (2021) 113728.

[26] Y. Wang, F. Han, G. Lubineau, Strength-induced peridynamic modeling and simulation of fractures in brittle materials, Comput. Methods Appl. Mech. Engrg. 374 (2021) 113558.

[27] H. Zhang, P. Qiao, L. Lu, Failure analysis of plates with singular and non-singular stress raisers by a coupled peridynamic model, Int. J. Mech. Sci. 157–158 (2019) 446–456.

[28] H. Zhang, P. Qiao, A coupled peridynamic strength and fracture criterion for open-hole failure analysis of plates under tensile load, Eng. Fract. Mech. 204 (2018) 103–118.

[29] W. Hu, Y.D. Ha, F. Bobaru, S.A. Silling, The formulation and computation of the nonlocal J-integral in bond-based peridynamics, Int. J. Fract. 176 (2012) 195–206.

[30] C. Stenström, K. Eriksson, The J-contour integral in peridynamics via displacements, Int. J. Fract. 216 (2019) 173–183.

[31] H. Zhang, P. Qiao, On the computation of energy release rates by a peridynamic virtual crack extension method, Comput. Methods Appl. Mech. Engrg. 363 (2020) 112883.

[32] H. Zhang, P. Qiao, Virtual crack closure technique in peridynamic theory, Comput. Methods Appl. Mech. Engrg. 372 (2020) 113318.

[33] D. Yang, X. He, X. Liu, Y. Deng, X. Huang, A peridynamics-based cohesive zone model (PD-CZM) for predicting cohesive crack propagation, Int. J. Mech. Sci. 184 (2020) 105830.

[34] D. Yang, X. He, S. Yi, X. Liu, An improved ordinary state-based peridynamic model for cohesive crack growth in quasi-brittle materials, Int. J. Mech. Sci. 153– 154 (2019) 402–415.

[35] Y. Tong, W. Shen, J. Shao, J. Chen, A new bond model in peridynamics theory for progressive failure in cohesive brittle materials, Eng. Fract. Mech. 223 (2020) 106767.

[36] W. Gerstle, N. Sau, S. Silling, Peridynamic modeling of concrete structures, Nucl. Eng. Des. 237 (2007) 1250–1258.

[37] D. Yang, W. Dong, X. Liu, S. Yi, X. He, Investigation on mode-I crack propagation in concrete using bond-based peridynamics with a new damage model, Eng. Fract. Mech. 199 (2018) 567–581.

[38] X. Gu, Q. Zhang, D. Huang, Y. Yv, Wave dispersion analysis and simulation method for concrete SHPB test in peridynamics, Eng. Fract. Mech. 160 (2016) 124–137.

[39] K. Zhang, T. Ni, G. Sarego, M. Zaccariotto, Q. Zhu, U. Galvanetto, Experimental and numerical fracture analysis of the plain and polyvinyl alcohol fiber-reinforced ultra-high-performance concrete structures, Theor. Appl. Fract. Mech. 108 (2020) 102566.

[40] W. Hu, Y.D. Ha, F. Bobaru, Peridynamic model for dynamic fracture in unidirectional fiber-reinforced composites, Comput. Methods Appl. Mech. Eng. 217–220 (2012) 247–261.

[41] Y. Hu, E. Madenci, Bond-based peridynamic modeling of composite laminates with arbitrary fiber orientation and stacking sequence, Compos. Struct. 153 (2016) 139–175.

[42] H. Zhang, P. Qiao, A state-based peridynamic model for quantitative elastic and fracture analysis of orthotropic materials, Eng. Fract. Mech. 206 (2019) 147–171.

[43] X. Zhou, Y. Wang, Q. Qian, Numerical simulation of crack curving and branching in brittle materials under dynamic loads using the extended non-ordinary state-based peridynamics, Eur. J. Mech. A/Solids. 60 (2016) 277–299.

[44] Y. Wang, X. Zhou, Y. Shou, The modeling of crack propagation and coalescence in rocks under uniaxial compression using the novel conjugated bond-based peridynamics, Int. J. Mech. Sci. 128–129 (2017) 614–643.

[45] B. Alali, M. Gunzburger, Peridynamics and material interfaces, J. Elasticity 120 (2015) 225–248.

[46] P. Seleson, M. Gunzburger, M.L. Parks, Interface problems in nonlocal diffusion and sharp transitions between local and nonlocal domains, Comput. Methods Appl. Mech. Engrg. 266 (2013) 185–204.

[47] F. Wang, L. Liu, Q. Liu, D. Cao, S. Yang, Studies of bimaterial interface fracture with peridynamics, in: Barcelona, 2014, pp. 1–9.

[48] H. Zhang, P. Qiao, An extended state-based peridynamic model for damage growth prediction of bimaterial structures under thermomechanical loading, Eng. Fract. Mech. 189 (2018) 81–97.

[49] S.A. Silling, M. Zimmermann, R. Abeyaratne, Deformation of a peridynamic bar, J. Elasticity 73 (2003) 173–190.

[50] Q.V. Le, F. Bobaru, Surface corrections for peridynamic models in elasticity and fracture, Comput. Mech. 61 (2018) 499–518.

[51] H. Ishikawa, A finite element analysis of stress intensity factors for combined tensile and shear loading by only a virtual crack extension, Int. J. Fract. 16 (1980) 243–246.

[52] F. Bobaru, M. Yang, L.F. Alves, S.A. Silling, E. Askari, J. Xu, Convergence, adaptive refinement, and scaling in 1D peridynamics, Internat. J. Numer. Methods Engrg. 77 (2009) 852–877.

[53] B. Kilic, E. Madenci, An adaptive dynamic relaxation method for quasi-static simulations using the peridynamic theory, Theor. Appl. Fract. Mech. 53 (2010) 194–204.

[54] M.L. Benzeggagh, M. Kenane, Measurement of mixed-mode delamination fracture toughness of unidirectional glass/ epoxy composites with mixed-mode bending apparatus, Compos. Sci. Technol. 56 (1996) 439–449.

[55] H. Zhong, E.T. Ooi, C. Song, T. Ding, G. Lin, H. Li, Experimental and numerical study of the dependency of interface fracture in concrete-rock specimens on mode mixity, Eng. Fract. Mech. 124–125 (2014) 287–309.